Spring 2005

The Straggling Green's Function Method for Ion Transport

Steven Andrew Walker
Old Dominion University

THE STRAGGLING GREEN'S FUNCTION METHOD FOR ION TRANSPORT

by

Steven Andrew Walker
B.S. May 1996, Old Dominion University

A Dissertation Submitted to the Faculty of
Old Dominion University in Partial Fulfillment of the
Requirement for the Degree of

DOCTOR OF PHILOSOPHY

COMPUTATIONAL AND APPLIED MATHEMATICS

OLD DOMINION UNIVERSITY
May 2005

Approved by:

John Tweed (Director)

Ram K. Tripathi (Member)

John Adam (Member)

Gordon Melrose (Member)

ABSTRACT

THE STRAGGLING GREEN'S FUNCTION METHOD FOR ION TRANSPORT

Steven Andrew Walker
Old Dominion University, 2005
Director: Dr. John Tweed

For many years work has been conducted on developing a concise theory and method for HZE ion transport capable of being validated in the laboratory. Previous attempts have ignored dispersion and energy downshift associated with nuclear fragmentation and energy and range straggling. Here we present a Green's function approach to ion transport that incorporates these missing elements. This work forms the basis for a new version of GRNTRN, a Green's function transport code. Comparisons of GRNTRN predictions and laboratory results for an ^{56}Fe ion beam with average energy at the target of one GeV/amu or more are presented for various targets. Quantities compared are the energy deposited spectra for an Aluminum target and Graphite-Epoxy mix target, the fraction of primary beam surviving and track average LET for these and various other targets.

ACKNOWLEDGMENTS

I would like to thank my advisor Dr. John Tweed for his time, patience and encouragement throughout my research and writing. I would like to thank my committee for their time and effort in reading and rereading the various versions of this manuscript and for their suggestions and advice on how to smooth out the rough edges and clarify things. I would like to thank the entire Math department for the family-like atmosphere they have created. I would especially like to thank the departmental secretaries, Mrs. Barbara Jeffrey and Mrs. Gayle Tarkelson, for the invaluable assistance they have rendered in cutting through red tape and other bits of bureaucratic snafu.

I would like to thank my friends and family, especially my parents, for their encouragement and understanding while I was at graduate school. Their son, the 'professional student', is finally graduating.

This research was supported under NASA Research Grant NCC-1-396 and NASA Research Grant NAG-1-03077. I would like to thank the radiation group headed by John Wilson of the Computational Structures and Materials Branch at NASA Langley Research Center for the funding and the assistance they have provided with this research. I would like to also thank Jack Miller and his group at the Lawrence Berkeley National Laboratory for sharing their experimental data with me.

TABLE OF CONTENTS

Page

Page

LIST OF TABLES

LIST OF FIGURES

CHAPTER I

INTRODUCTION

"Space, the final frontier... ". These curiously prophetic words are as true today as they were back in the mid 1960's. Then, man had the goal to go to the moon; today, the goal is to revisit the moon, and then send people to Mars. One of the critically important problems to be solved facing space exploration as mankind travels deeper into our solar system, and beyond, is that of radiation protection for people and electronics. The protection issue that most needs to be resolved relates to particle radiation, particularly protection from ions. Ions are formed when the electrons in an atom are removed, leaving the positively charged nucleus behind. The transport of ions presents the area of radiation shielding in need of the most development.

The first of three major sources of ions in space is the sun. The fusion process that powers the sun produces an outward ion flow known as the solar winds. Upon occasion there is an expulsion of solar matter from the sun's surface, called a solar flare. The largest, most violent events from the sun are coronal mass ejections, CME. Where the solar winds would be a light drizzle and the solar flares a heavy rain shower to thunderstorm, a CME would be a major hurricane. These solar particle events, SPE, (solar winds, flares, and CME) that strike earth are sometimes collectively denoted as solar rays or solar cosmic rays. The sun is also a contributor to the second major ion source, known as the van Allen belts. The van Allen belts are bands of ions and electrons trapped by the earth's magnetic field. While not occupying a large volume, parts of the

---

The model for this dissertation was Nuclear Instruments and Methods in Physics Research B: Beam Interactions with Materials and Atoms.

van Allen belts contain large numbers of particles and can be quite dangerous to humans and electronics. The third major ion source is galactic cosmic rays (GCR). These are ions that travel into the solar system from outside it. GCR sources are the winds, flares, and CME of other stars in the galaxy, the expulsion of matter as stars transition from one stage in their life cycle to another, and the explosion of stars known as novas (novae) and supernovas (supernovae). Solar cosmic rays typically have large fluences and relatively low energy, while galactic cosmic rays have low fluences and large energies. The fluence, or differential flux, is the number of particles moving in a given direction crossing one square cm of area per second with energy between E and $E+dE$. Of these cosmic rays, the high charge and energy (HZE) component is the focus of most research, due to HZE ions presenting the greatest health risk in space. On earth we are somewhat protected by the earth's magnetic field, creating the van Allen belts, and the atmosphere. In space, the only protection is what you take with you.

Brief History of Space Radiation Research

For a complete history of space radiation research, the reader is referred to the NASA publication *Transport Methods and Interactions for Space Radiations* [1]; what follows here is a brief summary up to its publication in 1991, and more detailed information on further developments since then.

In 1912, Hess' balloon experiments into atmospheric ionization led to the discovery of cosmic rays [2]. In 1948, Freier et al. found evidence for [3], and Freier, Lofgren, Ney, and Oppenheimer confirmed [4], a heavy ion component of cosmic rays in the Earth's upper atmosphere. A year later at the meeting "Aero Medical Problems of Space Travel", C. F. Gell stated that cosmic rays were a definite health risk, and

potentially could be fatal, despite the current belief to the contrary, and urged that space radiation protection be further investigated [5]. In 1950, Gell's concerns were verified by H. J. Schaefer, who's data showed that radiation rates were over 100 times higher in the upper atmosphere than at sea level [6].

In 1956 the then largest recorded solar flare event occurred. This event had a great influence on the direction of radiation shielding design and studies. It was decided at the 1960 Conference on Radiation Problems in Manned Space Flight that for short manned missions the GCR background was not deemed a large safety issue; the major concern was shielding against large SPE [7].

NASA Langley Research Center began studying space radiation in the late 1950's and continues this research today. The work gained prominence when the proposed U.S. Supersonic Transport Program (the precursor/ inspiration to today's hyper-x program) was begun in the early 1960's and when NASA Langley was tapped in 1964 to help resolve the FAA's concern over radiation issues for high altitude commercial air flights.

At that time, all the codes for radiation transport were based on Monte Carlo methods. The most widely used of these codes was HETC, High-Energy Transport Code, based at Oakridge National Laboratory. The computers of the day, combined with the Monte Carlo method, gave HETC a very long run time for computations. The long runs, combined with HETC's popularity, found Langley researchers waiting long times for code results. It was therefore decided that it would be advantageous to have a local transport code for Langley's work. This was the start of radiation code development at the NASA Langley Research Center. The first code developed, PROPER-C, and its successor, PROPER-3C, were Monte Carlo based codes. They gave Langley researchers

the results they needed, but still had long, and expensive, computation times.

In order to combat the long, expensive runs required for radiation calculations, researchers decided to switch from Monte Carlo based methods to deterministic methods in the mid 1970's. Deterministic methods use perturbation techniques, the "straightahead" approximation, and the velocity conserving approximation to solve Boltzmann's equation in one dimension. These methods have been the heart of transport development at the Langley Research Center for the last 30 years.

The first code developed at NASA Langley was BRYNTRN, baryon transport code, of the late 1980's [1,8,9]. This code could handle lighter particles at various energies, and was designed for space shielding computations with a solar source. These computations were fine for the moon era space missions, but would need to be augmented for proposed longer missions in low earth orbit, the continuing Supersonic Transport program, and sending probes to other planets in the solar system. For such missions, the GCR background radiation, which has a strong HZE component, would play a large role in shielding concerns.

Thus, after completion of BRYNTRN, researchers turned their attention to the transport of heavy ions. This culminated in the development of GCRTRN, Galactic Cosmic Ray transport code, for heavy ion transport in the space environment [10-12]. In the early 1990's, BRYNTRN and GCRTRN were combined into HZETRN, high charge and energy transport, a one dimensional code capable of shielding computations for any space environment [1,13,14]. All these codes use the straightahead approximation and a numerical marching scheme in transport computations. To support HZETRN, a series of semiempirical nuclear fragmentation models, HZEFRG1 and NUCFRG2, were

developed [15,16].

Laboratory Validation of Codes

It has long been recognized that any ion transport code needs to be validated with experimental results [17-19]. Codes based on numerical methods are fine in situations where radiation fields are smooth and slowly varying, like in space, but cannot handle situations where there are large variations in energy in a small area, like those occurring in a particle beam [20]. HZETRN is no exception to this. Only codes based on analytical methods have been identified to bridge this gap, with Green's functions methods being emphasized [21].

Work to use the Green's function methods for ion transport started in earnest in the 1970's. The first major effort was the Energy Independent Green's function method, first introduced by Wilson in 1977 [22]. This method formed the basis for the early versions of BRYNTRN, GCRTRN, and HZETRN [23]. The terms for the primary beam and the first generation fragments were derived [22], and Wilson later added the second generation fragment term in 1983 [11]. In this method nuclear cross section terms in Boltzmann's equation are replaced by constant values. Fragmentation is handled using the "velocity conserving" approximation, which states that fragments have the same velocity (energy) as the parent particle.

Energy Independent methods also formed the basis for the first attempts to produce a code for validation in the laboratory setting. While this code did enjoy some success in predicting experimental results [17], the limitations of the method were soon recognized. The assumption of energy independent nuclear cross sections is more appropriate in a space setting, and not for ion beams of the day. Most of the experiments

at that time were being done in the energy range of 400-600 MeV/amu. At these modest energies, the energy dependence of nuclear cross sections must be taken into account. Consequently, the Energy Dependent Green's function method was introduced, and the attenuation term and lowest order collision term were derived [17,24]. This method still incorporated the velocity conserving approximation. Once this method was introduced, NUCFRG2 was updated to generate the new energy dependent cross sections [25], and HZETRN was modified to use the new nuclear data [26]. With the inclusion of non-perturbative methods [1,27,28], the Energy Dependent method laboratory code, dubbed GRNTRN, for Green's function transport [23,29], was able to model several experiments with acceptable accuracy [29,30]. It was recognized that higher order collision terms needed to be derived for both the monoenergetic ion beam and Gaussian ion beam.

As time progressed, more detailed models were required to more accurately reflect ion transport through targets and detectors [19]. The greater desired accuracy required a re-examination of the assumptions used in the current models. The velocity conserving approximation is one component that could use improvement. In a real collision, energy is lost in liberating the fragment(s), typically leaving the remaining nuclei and the fragment nuclei in an excited state, which results in further energy loss. A second factor that a new model could better reflect is the broadening of a particle beam, called straggling, as it passes through the target. Both of these factors are of small importance in space applications, but are critical for accurate comparisons to accelerator experiments.

The resolution of these issues was slow in coming. The first to be accomplished was the creation of a simple model for energy losses and dispersions in the fragmentation

process, done by Tripathi, Townsend and Khan in 1994 [31]. This energy loss is referred to as collision energy downshift and the accompanying dispersion is the interaction energy width. A simple straggling model was not developed until 2002 by Wilson, Tweed, Tai and Tripathi [32]. A Green's function transport theory which incorporates energy downshift and straggling, dubbed here as the Energy Dependent Straggling Green's function method, was first introduced in 2002 by Tweed, Wilson and Tripathi [33,34]. Here the attenuation term and the first fragmentation term were derived.

Objective of this Dissertation

In this dissertation a concise theory of ion transport using Green's functions will be developed. Along the way, new notation will be introduced and utilized, replacing previous notation that becomes unwieldy as the theory is developed. The attenuation term will be introduced using the new notation, and a general procedure for determining a portion of the various collision terms will be derived. Based on this general procedure, the first fragmentation term will be re-derived. A semi-analytic approximate second collision term will be developed. The non-perturbative remainder will then be introduced, utilizing the Green's function terms developed here. A computer code based on the initial beam, first and second fragmentation term, and non-perturbative remainder will be used to generate numerical data to be compared with a large number of experiments. This code is a new version of GRNTRN, and again uses the NUCFRG2 nuclear database.

Chapter II introduces the Boltzmann transport equation, common perturbation expansions, and examines the cross sections terms, both before and after the straightahead approximation is used, and finishes with the one dimensional linear

Boltzmann equation. Chapter III recasts the one dimensional Boltzmann equation in operator notation, examines the various perturbation solutions, and sets up the Green's function problem for the Boltzmann operator. Chapter IV derives the 0^{th}, n^{th}, 1^{st}, and 2^{nd} generation Green's functions and non-perturbative reminder. Chapter V compares the results from GRNTRN with a host of experiments done with a primary beam of ^{56}Fe ions with energy at target of 1000 MeV/amu or more. Chapter VI will provide a summary, and outline further areas of potential research.

CHAPTER II

BOLTZMANN EQUATION

Ion transport is governed by the Boltzmann equation. Other applications of the Boltzmann equation are the behavior of fluids, and plasma physics, to name a few [35]. Due to their low energies, very short range, and negligible production of secondary particles, target fragments can be ignored. Thus we focus on the linear Boltzmann's equation for the projectile fragments, which takes the form [1]

$$\mathbf{\Omega}\cdot\nabla\phi_j(\mathbf{z},\mathbf{\Omega},E)=\sum_k\int\sigma_{jk}(\mathbf{\Omega},\mathbf{\Omega}',E,E')\phi_k(\mathbf{z},\mathbf{\Omega}',E')dE'd\mathbf{\Omega}'-\sigma_j(E)\phi_j(\mathbf{z},\mathbf{\Omega},E)\ , \quad (2.1)$$

where $\phi_j(\mathbf{z},\mathbf{\Omega},E)$ represents the flux of j type ions at position $\mathbf{z}$ moving in direction $\mathbf{\Omega}$ with energy E, $\sigma_j(E)$ is the total macroscopic cross section for a j type particle, and $\sigma_{jk}(\mathbf{\Omega},\mathbf{\Omega}',\mathbf{E},\mathbf{E}')$ is the macroscopic production cross section. The production cross section represents all the processes by which a k type ion moving in direction $\mathbf{\Omega}'$ with energy E' produces a j type ion moving in direction $\mathbf{\Omega}$ with energy E. The total cross section is then found by summing over all values of k.

Cross Sections

A cross section is an effective area an object presents a viewer, similar to the object's shadow. For example, from any angle, the cross section of a sphere is a circle. The cross section of a can is a rectangle if viewed directly from the side, a circle if viewed directly from the top or bottom, and looks differently if viewed from other angles. In nuclear physics, a cross section is a measure of the probability that an interaction will occur, and is a different value for different kinds of interactions. If an ion moves a

distance d, then the probability that it will have an interaction is $\sigma_j(E)d$. The macroscopic cross sections can be expanded in a series of physically perturbative terms as

$$\sigma_j(E) = \sigma_j^{at}(E) + \sigma_j^{el}(E) + \sigma_j^{r}(E), \tag{2.2}$$

where $\sigma_j^{at}(E)$ refers to interactions with atomic electrons, $\sigma_j^{el}(E)$ represents elastic nuclear scattering, and $\sigma_j^{r}(E)$ are the various nuclear reactions. The production cross section can likewise be expanded. In moving a distance of one centimeter through matter a projectile ion has many collisions with atomic electrons (~10^6) and a large number of elastic scattering collisions (~10^2-10^3), while nuclear reactions are separated by a fraction to several centimeters.

As an ion travels through ordinary matter and interacts with the electrons, it loses energy in discrete amounts called the atomic/molecular electron excitation energy levels, ε_n, measured in units of MeV. The corresponding atomic differential cross section, $\sigma_{jk}^{at}(\mathbf{\Omega},\mathbf{\Omega}',E,E')$, is modeled by

$$\sigma_{jk}^{at}(\mathbf{\Omega},\mathbf{\Omega}',E,E') = \sum_n \sigma_{j,n}^{at}(E)\delta_{jk}\delta(E-E'+\in_n)\delta(\mathbf{\Omega}\cdot\mathbf{\Omega}'-1)/(2\pi), \tag{2.3}$$

where δ_{jk} is the Kronecker delta, $\delta(\ )$ is the Dirac delta function, and $\in_n = \varepsilon_n / A_k$, A_k the mass of a k type particle, in atomic mass units (amu). The sum is over all possible electron excitation energy levels and the $,n$ subscript is to emphasize that this subscript does not refer to a particle species. Interactions with electrons do not change the ion's direction of travel; this is reflected in the $\delta(\mathbf{\Omega}\cdot\mathbf{\Omega}'-1)$ term. It should be noted that $\sum_n \sigma_{j,n}^{at}(E') = \sigma_j^{at}(E')$. Due to the large number of atomic collisions, the series of

discrete energy losses is customarily approximated as a smooth, continuous process. In this continuous slowing down approximation, the amount of energy lost in moving a distance dx is

$$-\frac{dE}{dx} = \tilde{S}_j(E). \tag{2.4}$$

The quantity $\tilde{S}_j(E)$ is the stopping power per unit mass, and is defined by

$$\tilde{S}_j(E) = \sum_n \sigma_{j,n}^{at}(E) \in_n . \tag{2.5}$$

Also from the continuous slowing down approximation can be derived the range/energy relationship,

$$R_j(E') = \int_0^{E'} \frac{de}{\tilde{S}_j(e)}, \tag{2.6}$$

which includes relativistic polarization effects [36], and its inverse, $R_j^{-1}(x)$, with $E = R_j^{-1}[R_j(E)]$. From (2.6) it can be seen that

$$\frac{dR_j(E)}{dE} = \frac{1}{\tilde{S}_j(E)}. \tag{2.7}$$

This derivative will be used extensively throughout this dissertation.

Fig. 1 gives a qualitative representation of the range/energy relationship. A particle strikes the target with initial energy E' and will travel a distance of $R_j(E')$, also referred to as R_0, before stopping. This distance is the range of the particle. After traveling a distance x, the particle has energy E remaining, and will travel a distance $R_j(E)$ more before it stops. The remaining energy, E, can be expressed in terms of the initial energy and the penetration depth. We thus define the function $E_j(x, E')$ as

$$E = E_j(x, E') \equiv R_j^{-1}\left[R_j(E') - x\right]; \tag{2.8}$$

that is, $E_j(x, E')$ represents the residual energy of a particle with initial energy E' after penetrating a depth x. In a similar way, we can define a function $\bar{E}_j(x, E)$ to represent the initial energy a particle had before it penetrated a distance x and has remaining energy E as

$$E' = \bar{E}_j(x, E) \equiv R_j^{-1}\left[R_j(E) + x\right]. \tag{2.9}$$

Both of these functions will be used extensively throughout this dissertation.

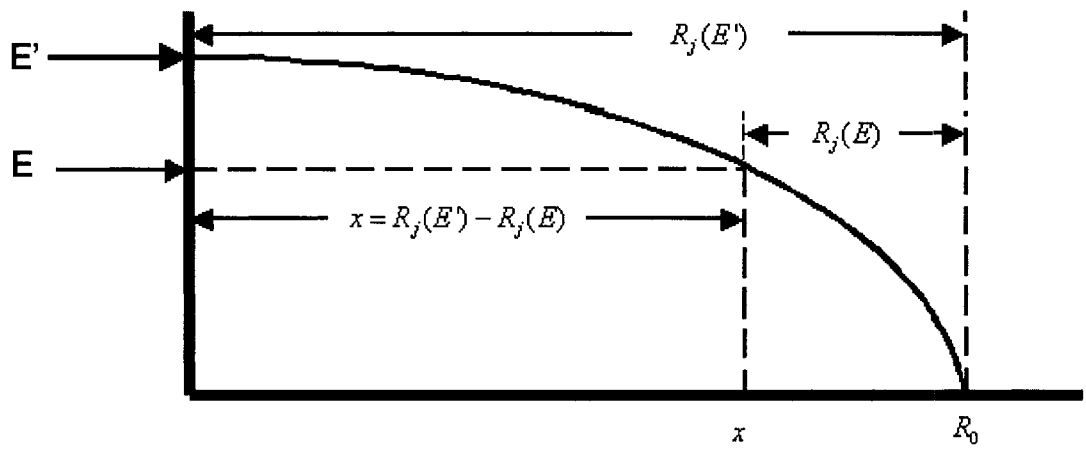

Fig. 1. Graphical representation of the range/ energy relationship and its inverse. The projectile has initial energy E' and after traveling a distance x has energy E.

Nuclear elastic scattering is when the total kinetic energy of the interacting ions is the same both before and after the interaction. The ions behave as if they were perfect billiard balls. The projectile ion is no longer traveling in the same direction as it was originally. The elastic scattering differential cross sections are modeled here by

$$\sigma_{jk}^{el}(\mathbf{\Omega}, \mathbf{\Omega}', E, E') = \sigma_j^{el}(\mathbf{\Omega}, \mathbf{\Omega}', E')\delta_{jk}\delta[E - f(E', \mathbf{\Omega} \cdot \mathbf{\Omega}')], \tag{2.10}$$

where $f(E', \mathbf{\Omega} \cdot \mathbf{\Omega}')$ is the elastic scattering energy function.

Nuclear reactions, while not numerous, are very important due to the large changes in energy and the production of fragment particles. The produced particles fall broadly into two major groups. The first group is the particles that are emitted in a small cone about the projected forward path of the projectile, referred to as the forward component. Typically, these particles are remnants of the projectile and have large energies and momenta. The second group is all the remaining particles, called the isotropic component, because they are emitted isotropically about the struck nucleus. Most of these particles are neutrons and light ions of low energy.

While it is possible to split the nuclear reactive cross section into a forward and isotropic component, this will not be done. Due to the low energies of the particles, and consequently their short range, most of the isotropic component does not emerge from the target and will be ignored. Therefore, the differential cross section for the nuclear reactive process is approximated by

$$\sigma_{jk}^{r}(\mathbf{\Omega}, \mathbf{\Omega}', E, E') = \sigma_{j}^{r}(\mathbf{\Omega}, \mathbf{\Omega}', E') \exp[-(E + \lambda_{jk} - E')^2 / 2\varepsilon_{jk}^2] / \sqrt{2\pi}\varepsilon_{jk}, \quad (2.11)$$

where λ_{jk} is the collision energy downshift (MeV/amu) and ε_{jk} is the corresponding energy interaction width (MeV/amu) for the process by which a j type particle is produced when a k type particle collides with a target atom. The energy downshift and interaction width are approximated from known heavy ion interactions using a Gaussian model [31]. There λ_{jk} is approximated by

$$\lambda_{jk}(E) = \frac{p(E) p_s}{A_j (m + E)}, \quad (2.12)$$

where the momentum downshift, p_s, (MeV/c) is [31]

$$p_s = 3.64\left(9+\frac{A_j}{A_k}\right)\sqrt{\frac{9}{A_k^{1/3}}-\frac{5}{A_j^{2/3}}}-28, \tag{2.13}$$

A_k the projectile mass (amu), A_j is the fragment mass, E is the fragment energy, m is the energy equivalent of a proton mass, and

$$p(E)=\sqrt{E^2+2mE} \tag{2.14}$$

is the fragment momentum (MeV/amu/c). In a similar way, the interaction energy width is related to the momentum width σ_F (MeV/c) via

$$\varepsilon_{jk}(E)=\frac{p(E)\sigma_F}{A_j(m+E)}, \tag{2.15}$$

where σ_F is defined as [31]

$$\sigma_F=\sqrt{\frac{1}{2}m\left(\frac{45}{A_k^{1/3}}-\frac{25}{A_j^{2/3}}\right)\left(\frac{A_j\left(A_k-A_j\right)}{A_k-1}\right)}. \tag{2.16}$$

Straightahead Approximation and the One Dimensional Boltzmann Equation

The Boltzmann equation is a formidable equation to solve. That is why many investigators have used approximations to simplify the equation. In a series of papers, the first of which appeared in 1965, Alsmiller et al. [37] and Alsmiller, Irving and Moran [38], validated the straightahead approximation for use in space shielding applications. Since then, many investigators have used the straightahead approximation when solving the Boltzmann equation (see for example the introduction to chapter 9 in [1] for a partial list spanning 1965- 1990 and all the papers on Green's function methods cited in the introduction). The straightahead approximation simply states that any particles', and their fragments', direction is not changed by any nuclear interactions with the target

material. In one dimension, this would mean that projectile particles and all secondary particles travel in the same direction. Mathematically, this requirement takes the form

$$\mathbf{\Omega}\cdot\mathbf{\Omega}' = 1. \tag{2.17}$$

Further, we will require that the position vector $\mathbf{z}$ be of the form

$$\mathbf{z} = x\mathbf{\Omega}. \tag{2.18}$$

Thus, equation (2.1) reduces to the one dimensional linear Boltzmann equation

$$\frac{d\phi_j(x,E)}{dx} = \sum_k \int \sigma_{jk}(E,E')\phi_k(x,E')dE' - \sigma_j(E)\phi_j(x,E). \tag{2.19}$$

The solution of this equation is the focus of this dissertation.

The straightahead approximation also simplifies the cross sections. All the angular dependence for equations (2.10) and (2.11) is removed from the cross section terms and replaced by $\delta(\mathbf{\Omega}\cdot\mathbf{\Omega}-1)/(2\pi)$. With this, in one dimension, the angular dependence can be completely suppressed. Thus the elastic nuclear scattering differential cross section becomes

$$\sigma_{jk}^{el}(E,E') = \sigma_j^{el}(E')\delta_{jk}\delta(E-E') \tag{2.20}$$

and the nuclear reactive cross section is

$$\sigma_{jk}^{r}(E,E') = \sigma_j^{r}(E')\exp[-(E+\lambda_{jk}-E')^2/2\varepsilon_{jk}^2]/\sqrt{2\pi}\varepsilon_{jk}. \tag{2.21}$$

CHAPTER III

ATOMIC AND NUCLEAR PROCESSES

Atomic Process and the Atomic Green's Function

For convenience, Boltzmann's equation will be put into operator form. We thus introduce the vector field function,

$$\mathbf{\Phi} = [\phi_j(x,E)], \tag{3.1}$$

the drift operator,

$$\mathbf{D} = [\partial_x] \tag{3.2}$$

and interaction operator

$$\mathbf{I} = \mathbf{\Xi} - \boldsymbol{\sigma} = \left[\sum_k \int \sigma_{jk}(E,E')dE' - \sigma_j(E) \right]. \tag{3.3}$$

The interaction operator $\mathbf{I}$ has three parts corresponding to the atomic, elastic, and nuclear reactive processes as described in (2.2) and the section in chapter 2 on cross sections. Thus the Boltzmann equation (2.19) can be written as

$$[\mathbf{D} - \mathbf{I}^{at} - \mathbf{I}^{el} + \boldsymbol{\sigma}^r] \cdot \mathbf{\Phi} = \mathbf{\Xi}^r \cdot \mathbf{\Phi}. \tag{3.4}$$

Consider a stream of particles incident on a slab of some material target at location x'. To first approximation only the atomic terms in (2.2) contribute to the problem of finding the particle flux $\phi_j(x,E)$ and we must solve

$$\mathbf{D} \cdot \mathbf{\Phi} = \mathbf{I}^{at} \cdot \mathbf{\Phi}. \tag{3.5}$$

Using the continuous slowing down approximation (2.4), (3.5) can be written out as

$$\frac{\partial \phi_j(x,E)}{\partial x} - \frac{\partial}{\partial E}[\tilde{S}_j(E)\phi_j(x,E)] = 0 \quad x > x', E > 0, \tag{3.6}$$

subject to the boundary condition

$$\phi_j(x',E) = F_j(E)\,. \tag{3.7}$$

The atomic problem is solved by a change of variables and then the method of characteristics with the resulting solution [39]

$$\phi_j(x,E) = \frac{\tilde{S}_j[\bar{E}_j(x-x',E)]}{\tilde{S}_j(E')} F_j(\bar{E}_j)\,, \tag{3.8}$$

$\bar{E}_j(x-x',E') = R_j^{-1}[R_j(E')+(x-x')]\,.$

In the special case of $F_j(E) = \delta_{jk}\delta(E-E')$, the resulting solution for $\phi_j(x,E)$ is the atomic Green's function, $G_{jk}^{at}(x,x',E,E')$,

$$G_{jk}^{at}(x,x',E,E') = \frac{S_j[\bar{E}_j(x-x',E)]}{S_j(E')}\delta_{jk}\delta[\bar{E}_j(x-x',E)-E']\,. \tag{3.9}$$

Using (2.4), (2.7) and the relationship $\delta(y-y_0) = \delta[f(y)-f(y_0)]f'(y_0)$, the atomic Green's function can be simplified to

$$G_{jk}^{at}(x,x',E,E') = \delta_{jk}\delta[E-E_j(x-x',E')]\,. \tag{3.10}$$

Nuclear Elastic Scattering

Nuclear elastic scattering requires the solution of

$$[\mathbf{D}-\mathbf{I}^{at}]\cdot\mathbf{\Phi} = \mathbf{I}^{el}\cdot\mathbf{\Phi}\,. \tag{3.11}$$

Due to the assumed form of the elastic scattering cross sections (2.20),

$$\mathbf{I}^{el}\cdot\mathbf{\Phi} \approx \mathbf{0}\,; \tag{3.12}$$

that is, in the approximation being considered, elastic scattering does not contribute to the solution. This is a consequence of the straightahead approximation coupled with Boltzmann's equation being considered in only one dimension.

Nuclear Reactive Processes

For nuclear reactive processes, Boltzmann's equation takes the form

$$[\mathbf{D}-\mathbf{I}^{at}+\boldsymbol{\sigma}^{r}]\cdot\boldsymbol{\Phi}=\boldsymbol{\Xi}^{r}\cdot\boldsymbol{\Phi}, \tag{3.13}$$

with boundary condition $\boldsymbol{\Phi}_B=[F_j(E)]$. The technique used to solve the atomic problem enables us to recast (3.13) as an integral equation, which in operator form is

$$\boldsymbol{\Phi}=[\mathbf{D}-\mathbf{I}^{at}+\boldsymbol{\sigma}^{r}]^{-1}\cdot\boldsymbol{\Phi}_B+\int_{x'}^{x}[\mathbf{D}-\mathbf{I}^{at}+\boldsymbol{\sigma}^{r}]^{-1}\cdot\boldsymbol{\Xi}^{r}\cdot\boldsymbol{\Phi}\,d\xi\,. \tag{3.14}$$

The solution to the homogenous form of (3.13),

$$[\mathbf{D}-\mathbf{I}^{at}+\boldsymbol{\sigma}^{r}]\cdot\boldsymbol{\Phi}_B=\mathbf{0}, \tag{3.15}$$

with a single particle incident at the boundary, is the zero order Green's function for this problem, and is denoted as $\mathbf{G}^0$. Equation (3.14) can be rewritten as

$$\boldsymbol{\Phi}=\mathbf{G}^0\cdot\boldsymbol{\Phi}_B+\mathbf{Q}\cdot\mathbf{G}^0\cdot\boldsymbol{\Xi}^{r}\cdot\boldsymbol{\Phi}, \tag{3.16}$$

which is a Volterra integral equation and can be solved as a Neumann series as [1,34]

$$\begin{aligned}\boldsymbol{\Phi}&=[\mathbf{G}^0+\mathbf{Q}\cdot\mathbf{G}^0\cdot\boldsymbol{\Xi}^{r}\cdot\mathbf{G}^0+\mathbf{Q}\cdot\mathbf{G}^0\cdot\boldsymbol{\Xi}^{r}\cdot\mathbf{Q}\cdot\mathbf{G}^0\cdot\boldsymbol{\Xi}^{r}\cdot\mathbf{G}^0+\ldots]\cdot\boldsymbol{\Phi}_B\\&=[\mathbf{G}^0+\mathbf{G}^1+\mathbf{G}^2+..]\cdot\boldsymbol{\Phi}_B\,.\end{aligned} \tag{3.17}$$

This series has a physical interpretation. The $\mathbf{G}^0\cdot\boldsymbol{\Phi}_B$ term propagates the initial beam from the boundary to the target interior. The production density of the first generation of secondary (daughter) particles at the point ξ is represented by $\boldsymbol{\Xi}^{r}\cdot\mathbf{G}^0\cdot\boldsymbol{\Phi}_B$. These particles are then propagated through the target by $\mathbf{G}^0\cdot\boldsymbol{\Xi}^{r}\cdot\mathbf{G}^0\cdot\boldsymbol{\Phi}_B$, and then $\mathbf{G}^1\cdot\boldsymbol{\Phi}_B=\mathbf{Q}\cdot\mathbf{G}^0\cdot\boldsymbol{\Xi}^{r}\cdot\mathbf{G}^0\cdot\boldsymbol{\Phi}_B$ sums the propagated particles in the interval $[x,x']$. A corresponding interpretation exists for the higher order terms. It is important to note the relationship [1,34]

$$\mathbf{G}^{n+1} = [\mathbf{Q} \cdot \mathbf{G}^0 \cdot \Xi^r] \cdot \mathbf{G}^n, \; n \geq 0, \tag{3.18}$$

which, in principle, enables us to compute the Neumann series recursively.

CHAPTER IV

THE GREEN'S FUNCTIONS

A Green's function, also called a response function or influence function, is the solution to a differential equation with a delta function source term. It represents a system's response to a single point source. A Green's function is specific to the equation, boundary conditions and geometry from which it is derived; change one of these factors and the Green's function changes. The power of this solution method is that once the Green's function is found, the solution for an arbitrary nonhomogenous term can be found by multiplying it by the Green's function and integrating the product over the appropriate region. For our purposes, if $H_j(E)$ is an arbitrary boundary condition and $G_{jk}(x,x',E,E')$ is the Green's function, then the solution becomes

$$\phi_j(x,E) = \sum_k \int_{-\infty}^{\infty} G_{jk}(x,x',E,F) H_k(F) dF \tag{4.1}$$

The Zero Order Green's Function

In the previous chapter, we demonstrated that the operator $\mathbf{G}^0$, called the zero order Green's function, and the reactive integral operator, Ξ^r, are all that are needed to construct the Neumann series (3.17). We already have Ξ^r; all that remains is to find $\mathbf{G}^0$.

As in the atomic problem, we take the boundary condition to be $F_j(E) = \delta_{jk}\delta(E-E')$. Not surprisingly, the solution is similar to the atomic problem, and $\mathbf{G}^0$ is found to be [34]

$$G^0_{jk}(x,x',E,E') = \frac{P_j(E')}{P_j(E)} \delta_{jk} \delta[E - E_k(x-x',E')]. \tag{4.2}$$

The nuclear attenuation factor, $P_j(E)$, is defined to be [1]

$$P_j(E) = \exp\left[-\int_0^E \frac{\sigma_j^r(\varepsilon)}{\tilde{S}_j(\varepsilon)} d\varepsilon\right], \tag{4.3}$$

and results from the factor of $\sigma_j^r(E)$ in equation (3.15).

In all the processes described so far, a delta function has been the input, and a delta function has been the output. This is not physically realistic. One would expect that as the ions move through the target some would lose more energy than others due to the inherent randomness of the actual atomic and nuclear processes. The delta function should represent the average energy at a depth $x - x'$, with an appropriate spread about this mean. To this end, we take the boundary delta function to be represented by a Gaussian

$$\delta(E-E') = \lim_{s_j(x,E)\to 0} \frac{1}{\sqrt{2\pi} s_j(x,E)} \exp\left[-\frac{(E-E')^2}{2s_j(x,E)^2}\right], \tag{4.4}$$

where the term $s_j(x,E)$ is the energy straggling parameter [32]. Utilizing this, $G_{jk}^0(x,x',E,E')$ now takes the form

$$G_{jk}^0(x,x',E,E') = \frac{\delta_{jk}}{\sqrt{2\pi} s_k(x-x',E')} \frac{P_k[E']}{P_k[E]} \exp\left\{-\frac{[E-E_k(x-x',E')]^2}{2s_k(x-x',E')^2}\right\}. \tag{4.5}$$

In a laboratory setting, a particle beam is not completely monoenergetic, but rather has the form of a highly peaked Gaussian about the beam energy. This would correspond to a boundary condition of the form

$$\phi_B(F) = \left[\frac{1}{\sqrt{2\pi} s'} \exp\left\{-\frac{(F-E')}{2s'^2}\right\}\right], \tag{4.6}$$

s' is the initial root mean square (rms) beam spread. The Green's function for this

boundary condition can be found from $\mathbf{G}^{\mathbf{b}} = \mathbf{G}^{0} \cdot \Phi_{B}$ as

$$G_{jk}^{b}(x,x',E,E') = \int_{-\infty}^{\infty} \frac{\delta_{jk}}{\sqrt{2\pi}s_k(x-x',F)} \frac{P_k[F]}{P_k[E]} \exp\left\{-\frac{[E-E_k(x-x',F)]^2}{2s_k(x-x',F)^2}\right\}$$

$$\cdot \frac{1}{\sqrt{2\pi}s'} \exp\left\{-\frac{(F-E')^2}{2s'^2}\right\} dF \,. \tag{4.7}$$

This integral may be approximated using saddle point technique as

$$G_{jk}^{b}(x,x',E,E') = \frac{\delta_{jk}}{\sqrt{2\pi}s_k^{b}(x-x',E')} \frac{P_k[E']}{P_k[E]} \exp\left\{-\frac{[E-E_k(x-x',E')]^2}{2s_k^{b}(x-x',E')^2}\right\}, \tag{4.8}$$

where

$$s_k^{b}(x-x',E')^2 = s_k(x-x',E')^2 + s'^2 r_k^{\,2}(x-x',E')^2, \tag{4.9}$$

$$r_k(x-x',E') = \frac{\tilde{S}_k[E_k(x-x',E')]}{\tilde{S}_k[E']}. \tag{4.10}$$

As expected, $\mathbf{G}^{b}$ reduces to $\mathbf{G}^{0}$ when s' approaches zero. For the rest of this work, the straggling form of $\mathbf{G}^{0}$ will be used, as will the Gaussian boundary condition Green's function $\mathbf{G}^{b}$.

Fig. 2 shows the computed $\mathbf{G}^{0}$ term for a monoenergetic beam and a Gaussian beam of ^{56}Fe, with initial energy of 1000 MeV/amu, at various depths in an aluminum slab. The depths, x/R_0, are expressed as fractions of the projectile's range. The solid line is the monoenergetic beam, and the dashed line is the Gaussian beam, with an initial spread of 5 MeV/amu. The attenuation of both beams is clearly evident. The Gaussian beam attenuates at a slower rate due to the initial beam spread. It should be noted that as both beams propagate, the beam widens. The effects of the initial spread to broaden a

beam are also evident. These effects will not necessarily be as prominent for higher order terms and their resulting fragments.

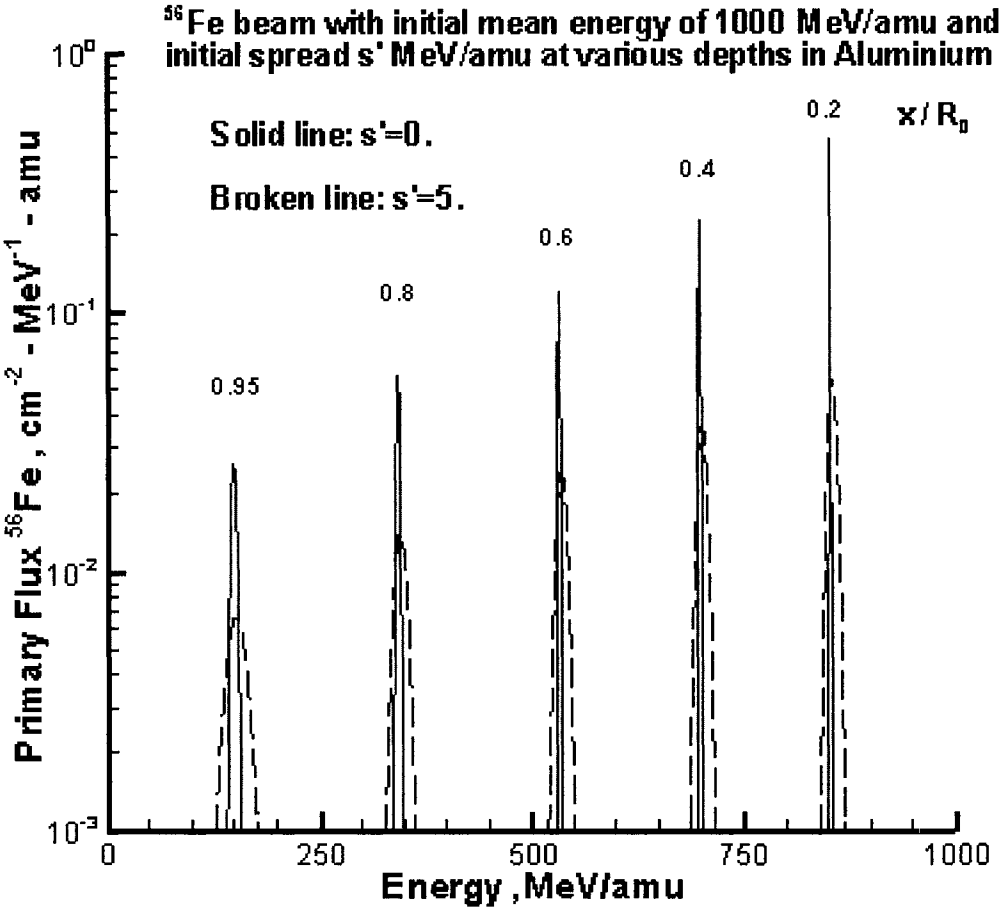

Fig. 2. Computed Zero Order Green's Function for an iron beam at various depths in Aluminum. The solid line is for a monoenergetic beam, $s' = 0$, and the dashed line is for a Gaussian beam, $s' = 5$ MeV/amu. The effects of straggling and attenuation are clearly apparent.

The Nth Order Green's Function

Now that we have identified $\mathbf{G}^0$, the relationship between $\mathbf{G}^{n+1}$ and $\mathbf{G}^n$ can be found via the recurrence relationship (3.18). Writing this out we have

$$G_{jk}^{n}(x,x',E,E') = \int_{x'}^{x}\int_{-\infty}^{\infty} G_{jj}^{0}(x,\xi,E,F)\left\{\sum_{p=j+1}^{k-1}\int_{-\infty}^{\infty}\sigma_{jp}^{r}(F,H)G_{pk}^{n-1}(\xi,x',H,E')dH\right\}dFd\xi \quad (4.11)$$

Utilizing (4.5) and (2.21), this can be expanded out to

$$G_{jk}^{n}(x,x',E,E') = \int_{x'}^{x}\int_{-\infty}^{\infty}\frac{P_j[F]}{P_j[E]}\frac{1}{\sqrt{2\pi}s_j(x-\xi,F)}\exp\left\{-\frac{\left[E-E_j(x-\xi,F)\right]^2}{2s_j(x-\xi,F)^2}\right\}$$

$$\cdot\left\{\sum_{p}\int_{-\infty}^{\infty}\sigma_{jp}^{r}(H)\frac{1}{\sqrt{2\pi}\varepsilon_{jp}}\exp\left\{-\frac{(F+\lambda_{jp}(F)-H)^2}{2\varepsilon_{jp}(F)^2}\right\}G_{pk}^{n-1}(\xi,x',H,E')dH\right\}dFd\xi \quad (4.12)$$

It is important to note that the integration with respect to the variable F can be done independently of the other variables. We thus separate it out as

$$I_F = \int_{-\infty}^{\infty}\frac{P_j[F]}{P_j[E]}\exp\left\{-\frac{[E-E_j(x-\xi,F)]^2}{2s_j(x-\xi,F)^2}\right\}\frac{\sigma_{jp}^{r}(H)}{\sqrt{2\pi}s_j(x-\xi,F)}$$

$$\cdot\exp\left[-\frac{(E_2+\lambda_{jp}(F)-H)^2}{2\varepsilon_{jp}{}^2(F)}\right]\frac{dF}{\sqrt{2\pi}\varepsilon_{jp}(F)}. \quad (4.13)$$

The first Gaussian reaches its maximum value when $E = E_j(x-\xi,F)$, or equivalently when

$$F = \bar{E}_j(x-\xi,E). \quad (4.14)$$

It is at this value of F the slowly varying terms of P_j, s_j, and ε_{jp} will be evaluated.

Next, $E_j(x-\xi,F)$ will be approximated by a truncated Taylor series about (4.14) by

$$E_j(x-\xi,F) \approx E_j(x-\xi,\bar{E}_j)+[\partial_F E_j(x-\xi,F)]_{\bar{E}_j}(F-\bar{E}_j)$$

$$= E+(F-\bar{E}_j)/\rho_j(x-\xi,\bar{E}_j), \quad (4.15)$$

where

$$\rho_j(x-\xi,\bar{E}_j) = S_j[\bar{E}_j]/S_j[E]. \quad (4.16)$$

Putting this all together, we get the following expression for $G^n_{jk}(x,x',E,E')$

$$G^n_{jk}(x,x',E,E') = \sum_p \int_{x'}^{x} \int_{-\infty}^{\infty} C_{jp}[x,\xi,E,H] \frac{G^{n-1}_{pk}(\xi,x',H,E')}{\sqrt{2\pi} a_{jp}(x-\xi,\bar{E}_j)}$$

$$\cdot \exp\left[-\frac{(H-\{\bar{E}_j + \lambda_{jp}(\bar{E}_j)\})^2}{2a_{jp}(x-\xi,\bar{E}_j)^2} \right] dH d\xi, \quad n \geq 1, \tag{4.17}$$

where

$$C_{jp}[x,\xi,E,H] = \frac{P_j[\bar{E}_j] S_j[\bar{E}_j]}{P_j[E] S_j[E]} \sigma^r_{jp}[H] \tag{4.18}$$

and

$$a_{jp}(x-\xi,\bar{E}_j)^2 = \rho_j(x-\xi,\bar{E}_j)^2 s_j(x-\xi,\bar{E}_j)^2 + \varepsilon_{jp}(\bar{E}_j)^2 . \tag{4.19}$$

The procedures outlined here will be used to find higher order terms in the expansion.

The First Order Green's Function

The first order Green's function for a laboratory beam can be found from $\mathbf{G}^1 = [\mathbf{Q} \cdot \mathbf{G}^0 \cdot \boldsymbol{\Xi}^r] \cdot \mathbf{G}^b$. To find that for a monoenergetic beam simply let the initial beam spread go to zero. Using the results from the n^{th} order Green's function, this can be expanded as

$$G^1_{jk}(x,x',E,E') = \int_{x'}^{x} \int_{-\infty}^{\infty} \frac{C_{jk}[x,\xi,E,F]}{\sqrt{2\pi} a_{jk}(x-\xi,\bar{E}_j)} \exp\left[-\frac{(F-\{\bar{E}_j + \lambda_{jp}(\bar{E}_j)\})^2}{2a_{jp}{}^2(x-\xi,\bar{E}_j)} \right]$$

$$\cdot \frac{P_k[E']}{P_k[F]} \exp\left\{ -\frac{[F-E_k(\xi-x',E')]^2}{2s^b_k(\xi-x',E')^2} \right\} \frac{dF d\xi}{\sqrt{2\pi} s^b_k(\xi-x',E')} . \tag{4.20}$$

Similar to what was done to derive the n^{th} order Green's function, the integration with respect to F can be approximated by evaluating the slowly varying terms at E_k and then integrating the remaining Gaussian product over all energy. This yields

$$G^1_{jk}(x,x',E,E') = \int_{x'}^{x} \frac{A_{jk}(\xi)}{\sqrt{2\pi}s_{jk}(\xi)} \exp\left\{-\frac{g_{jk}(\xi)^2}{2s_{jk}(\xi)^2}\right\} d\xi\,, \tag{4.21}$$

where, explicitly demonstrating the dependence on ξ,

$$g_{jk}(\xi) = g_{jk}[x,x',E,E';\xi] = E_k\left(\xi - x', E'\right) - \overline{E}_j(x-\xi,E) - \lambda_{jk}[\overline{E}_j(x-\xi,E)], \tag{4.22}$$

$$\begin{aligned} A_{jk}(\xi) &= A_{jk}[x,x',E,E';\xi] \\ &= \frac{P_j[\overline{E}_j(x-\xi,E)]P_k[E']S_j[\overline{E}_j(x-\xi,E)]}{P_j[E]P_k[E_k(\xi-x',E')]S_j[E]}\sigma^r_{jk}[E_k(\xi-x',E')]\end{aligned}, \tag{4.23}$$

and

$$s_{jk}(\xi)^2 = s_{jk}[x,x',E,E';\xi]^2 = a_{jp}\{x-\xi,\overline{E}_j(x-\xi,E)\}^2 + s^b_k(\xi-x',E')^2. \tag{4.24}$$

In order to perform the integration in (4.21) we will once again evaluate slowly varying terms at the peak of the Gaussian, which occurs when $g_{jk}(\xi) = 0$. This value, x_m, can be found using standard root finding techniques. Upon integrating the resulting simplified expression for (4.21), we find that

$$G^1_{jk}(x,x',E,E') \approx \frac{A_{jk}(x_m)}{2g_{jk}(x_m)'}\left\{erf\left[\frac{g_{jk}(x)}{\sqrt{2}s_{jk}(x_m)}\right] - erf\left[\frac{g_{jk}(x')}{\sqrt{2}s_{jk}(x_m)}\right]\right\}, \tag{4.25}$$

where the ' in $g_{jk}(x_m)'$ signifies a derivative. When there is no ambiguity about a derivative this convention will be used through out; otherwise the derivative will be explicitly stated.

Figs. 3 through 6 show a comparison between analytical and numerical approximations to the fluences of the first generation of ^{40}Ca and ^{16}O fragments for a 1000 MeV/amu beam of ^{56}Fe with an initial width of 0.0 or 5.0 MeV/amu at various depths in an aluminum target. The solid line is for numerical integration and the broken

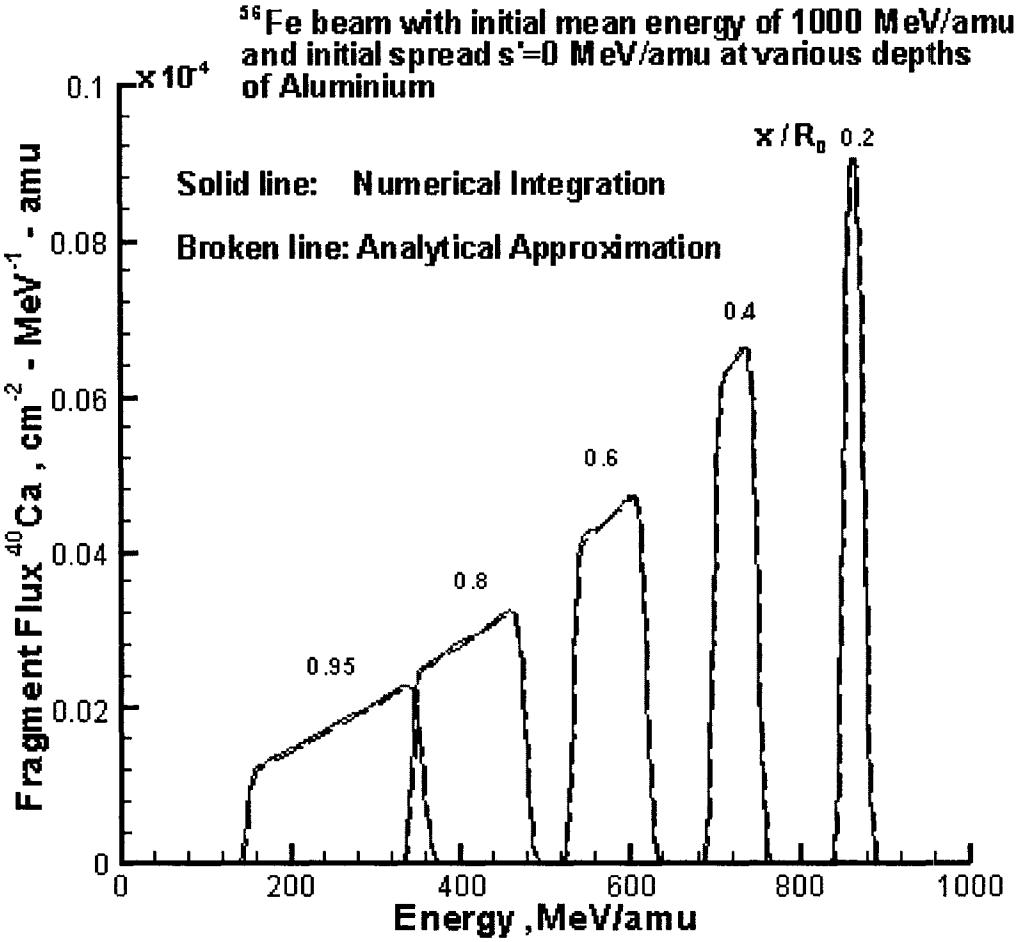

Fig. 3. First generation ^{40}Ca fragment flux at various depths for the case $s' = 0$. The solid line is from numerical integration, and the broken line is the first order Green's function.

line is for the analytic approximation in all these figures. The agreement between the two is quite good, even at large depths. A comparison between the figures with $s' = 0$ and $s' = 5$ shows the effects of the initial spread on the amplitude and width rather clearly for the ^{40}Ca fragments at all depths, but for ^{16}O the effects are mostly lost at large depths, and only show up clearly at small depths.

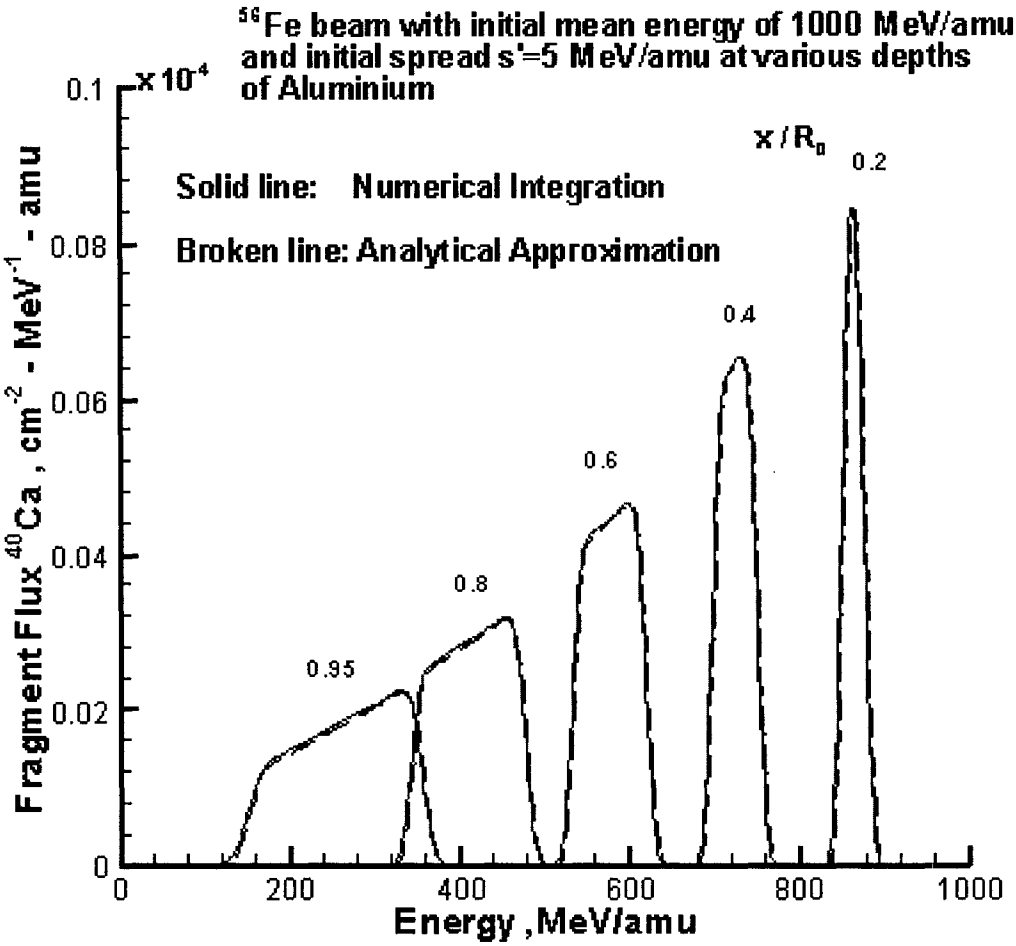

Fig. 4. First generation ^{40}Ca fragment flux at various depths for the case $s' = 5$. The solid line is from numerical integration, and the broken line is the first order Green's function.

The Second Order Green's Function

The second order Green's function can be found from the relationship

$\mathbf{G}^2 = [\mathbf{Q} \cdot \mathbf{G}^0 \cdot \Xi'] \cdot \mathbf{G}^1$, which expands out to

$$G_{jk}^2(x,x',E,E') = \sum_{p=j+1}^{k-1} \int_{x'}^{x} \int_{-\infty}^{\infty} \frac{C_{jp}[x,\xi,E,F]}{\sqrt{2\pi}a_{jp}(x-\xi,\bar{E}_j)} \int_{x'}^{\xi} \frac{A_{pk}[\xi,x',F,E';\eta]}{\sqrt{2\pi}s_{pk}[\xi,x',F,E';\eta]}$$
$$\cdot \exp\left\{-\frac{g_{pk}[\xi,x',F,E';\eta]^2}{2s_{pk}[\xi,x',F,E';\eta]^2}\right\} \exp\left[-\frac{(F-\{\bar{E}_j+\lambda_{jp}(\bar{E}_j)\})^2}{2a_{jp}{}^2(x-\xi,\bar{E}_j)}\right] d\eta dF d\xi . \qquad (4.26)$$

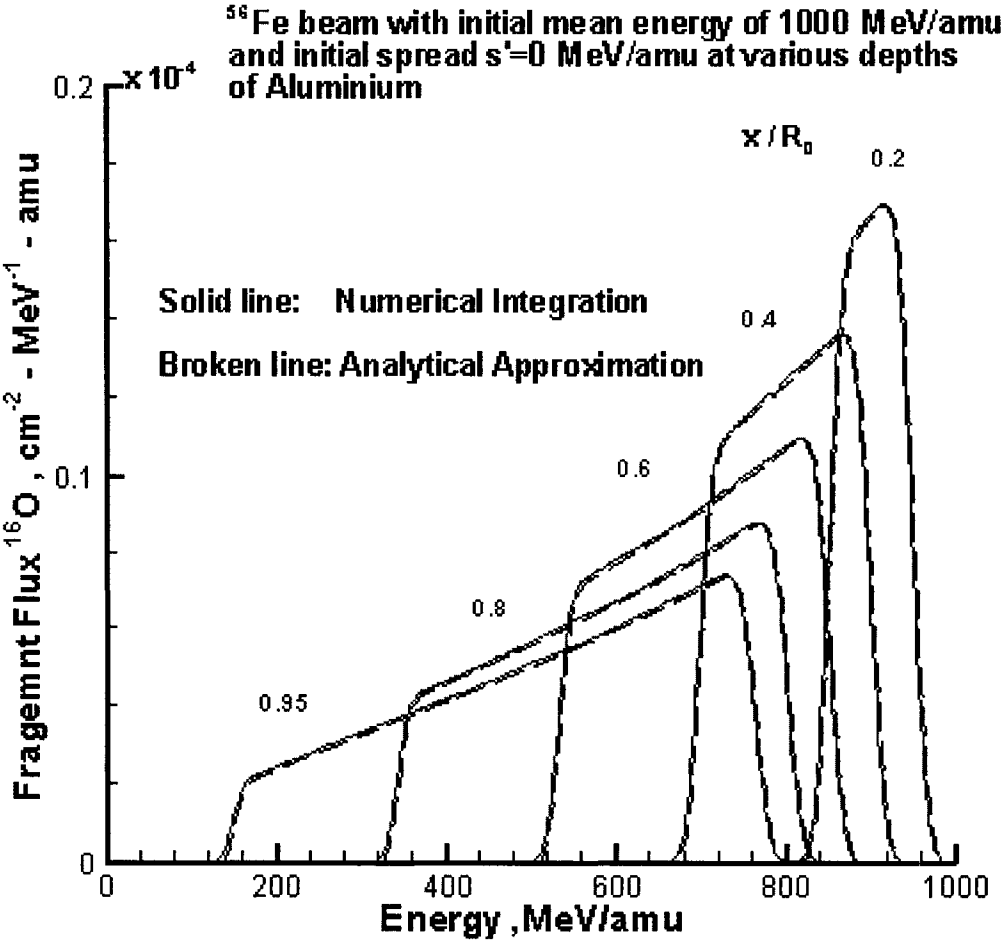

Fig. 5. First generation ^{16}O fragment flux at various depths for the case $s' = 0$. The solid line is from numerical integration, and the broken line is the first order Green's function.

The first step in approximating this integral is to evaluate terms slowly varying in energy at the peak of the second Gaussian in (4.26). This peak occurs at $F = \hat{E} = \bar{E}_j + \lambda_{jp}(\bar{E}_j)$.

Thus $G^2_{jk}(x, x', E, E')$ is approximately

$$G^2_{jk}(x,x',E,E') = \sum_{p=j+1}^{k-1} \int_{x'}^{x} \int_{x'}^{\xi} C_{jp}[x,\xi,E,\hat{F}] A_{pk}[\xi,x',\hat{E},E';\eta] \int_{-\infty}^{\infty} \exp\left\{ -\frac{g_{pk}[\xi,x',\hat{E},E';\eta]^2}{2s_{pk}[\xi,x',\hat{E},E';\eta]^2} \right\}$$
$$\cdot \frac{1}{\sqrt{2\pi} s_{pk}[\xi,x',\hat{E},E';\eta]} \exp\left[-\frac{(F-\hat{E})^2}{2a_{jp}(x-\xi,\bar{E}_j)^2} \right] \frac{dF d\eta d\xi}{\sqrt{2\pi a_{jp}(x-\xi,\bar{E}_j)}}. \qquad (4.27)$$

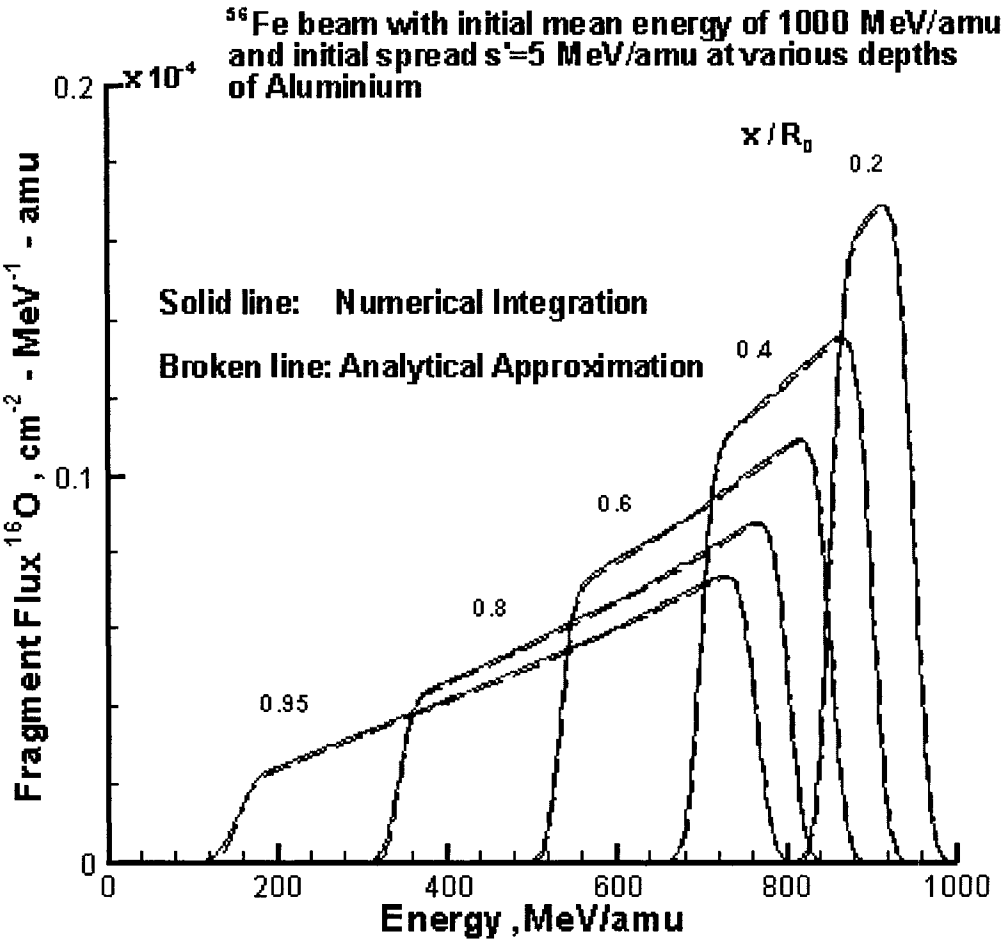

Fig. 6. First generation ^{16}O fragment flux at various depths for the case $s' = 5$. The solid line is from numerical integration, and the broken line is the first order Green's function.

The next step in approximating the energy integral is to expand g_{pk} in a Taylor series about $\hat{E}$ as

$$g_{pk}[\xi, x', F, E'; \eta] \approx g_{pk}[\xi, x', \hat{E}, E'; \eta] = -\{1 + \lambda_{pk}[\overline{E}_p(\xi - \eta, \hat{E})]'\}\rho_p[\overline{E}_p(\xi - \eta, \hat{E})](F - \hat{E}) \quad (4.28)$$

With this expansion, the energy integral in (4.27) can be done approximately, resulting in the following expression for $G^2_{jk}(x, x', E, E')$,

$$G_{jk}^2(x,x',E,E') \approx \sum_{p=j+1}^{k-1} \int_{x'}^{x} \int_{x'}^{\xi} C_{jp}[x,\xi,E,\hat{E}] A_{pk}[\xi,x',\hat{E},E';\eta]$$

$$\cdot \exp\left[-\frac{g_{pk}[\xi,x',\hat{E},E';\eta]^2}{2a_{jpk}(\xi,\eta)^2} \right] \frac{d\eta d\xi}{\sqrt{2\pi} a_{jpk}(\xi,\eta)}, \tag{4.29}$$

where

$$a_{jpk}^2(\xi,\eta) = a_{jpk}^2[x,x',E,E';\xi,\eta] = s_{pk}[\xi,x',\hat{E},E';\xi]^2$$

$$+\{1+\lambda_{pk}[\bar{E}_p(\xi-\eta,\hat{E})]'\}^2 \rho_p[\bar{E}_p(\xi-\eta,\hat{E})]^2 a_{jp}{}^2(x-\xi,\bar{E}_j). \tag{4.30}$$

After integrating over energy, all that remains is to perform the two spatial integrals. To accomplish this, we first let $x^* = (x+x')/2$ be chosen as a suitable mean value for the variable ξ. We now let $\eta = x_m^* = x_m^*(x^*)$ be the root of

$$g_{pk}[x^*,x',\hat{E},E';\eta] = 0. \tag{4.31}$$

We then evaluate slowly varying terms at these values of ξ and η, and integrate the remaining term with respect to η, yielding

$$G_{jk}^2(x,x',E,E') \approx \sum_{p=j+1}^{k-1} C_{jpk}[x^*,\hat{E},x_m^*] \int_{x'}^{x} \left\{ erf\left[\frac{w_1(\xi)}{\sqrt{2}s_{jpk}} \right] - erf\left[\frac{w_2(\xi)}{\sqrt{2}s_{jpk}} \right] \right\} d\xi, \tag{4.32}$$

where

$$w_1(\xi) = g_{pk}[\xi,x',\hat{E},E';\xi], \tag{4.33}$$

$$w_2(\xi) = g_{pk}[\xi,x',\hat{E},E';x'], \tag{4.34}$$

$$s_{jpk} = a_{jpk}(x^*,x_m^*) \tag{4.35}$$

and

$$C_{jpk}[x^*,\hat{E},x_m^*] = \frac{C_{jp}[x,x^*,E,\hat{E}] A_{pk}[x^*,x',\hat{E},E';x_m^*]}{2\{\partial_\eta g_{pk}[x^*,x',\hat{E},E';\eta]\}_{\eta=x_m^*}}. \tag{4.36}$$

Consider the integral $I^{(i)}$,

$$I^{(i)} = \int_{x'}^{x} erf\left[\frac{w_i(\xi)}{\sqrt{2}s_{jpk}}\right] d\xi \quad i = 1,2. \tag{4.37}$$

Let ζ_i be the root of $w_i(\xi) = 0$. We can approximate $w_i(\xi)$ by Taylor's theorem as

$$w_i(\xi) \approx w_i(\zeta_i) + (\xi - \zeta_i) w_i(\zeta_i)' = (\xi - \zeta_i) w_i(\zeta_i)', \tag{4.38}$$

and from differentiating (4.38) with respect to ξ, $w_i(\xi)' \approx w_i(\zeta_i)'$. Using these two relationships and integration by parts, we arrive at the following for $I^{(i)}$,

$$I^{(i)} = \frac{\sqrt{2}s_{jpk}}{w_i(\xi_i)'}\left\{\frac{w_i(x)}{\sqrt{2}s_{jpk}} erf\left[\frac{w_i(x)}{\sqrt{2}s_{jpk}}\right] - \frac{w_i(x')}{\sqrt{2}s_{jpk}} erf\left[\frac{w_i(x')}{\sqrt{2}s_{jpk}}\right]\right.$$

$$\left. + \frac{1}{\sqrt{\pi}}\exp\left[-\frac{w_i(x)^2}{2s_{jpk}^{\ 2}}\right] - \frac{1}{\sqrt{\pi}}\exp\left[-\frac{w_i(x')^2}{2s_{jpk}^{\ 2}}\right]\right\} \quad i = 1,2. \tag{4.39}$$

Using $I^{(i)}$, we arrive at the final form of $G_{jk}^2(x, x', E, E')$,

$$G_{jk}^2(x, x', E, E') = \sum_{j+1}^{k-1} C_{jp}(x^*, \hat{F}, x_m^*)\left[\frac{\sqrt{2}s_{jpk}}{w_1(\varsigma_1)'}\left\{\frac{w_1(x)}{\sqrt{2}s_{jpk}} erf\left[\frac{w_1(x)}{\sqrt{2}s_{jpk}}\right] - \frac{w_1(x')}{\sqrt{2}s_{jpk}} erf\left[\frac{w_1(x')}{\sqrt{2}s_{jpk}}\right]\right.\right.$$

$$\left. + \frac{1}{\sqrt{\pi}}\exp\left[-\frac{w_1(x)^2}{2s_{jpk}^{\ 2}}\right] - \frac{1}{\sqrt{\pi}}\exp\left[-\frac{w_1(x')^2}{2s_{jpk}^{\ 2}}\right]\right\} - \frac{\sqrt{2}s_{jpk}}{w_2(\varsigma_2)'}\left\{\frac{w_2(x)}{\sqrt{2}s_{jpk}} erf\left[\frac{w_2(x)}{\sqrt{2}s_{jpk}}\right]\right.$$

$$\left.\left. - \frac{w_2(x')}{\sqrt{2}s_{jpk}} erf\left[\frac{w_2(x')}{\sqrt{2}s_{jpk}}\right] + \frac{1}{\sqrt{\pi}}\exp\left[-\frac{w_2(x)^2}{2s_{jpk}^{\ 2}}\right] - \frac{1}{\sqrt{\pi}}\exp\left[-\frac{w_2(x')^2}{2s_{jpk}^{\ 2}}\right]\right\}\right]. \tag{4.40}$$

Figs. 7 through 10 show a comparison between analytical and numerical approximations to the fluences of the second generation of ^{40}Ca and ^{16}O fragments for a 1000 MeV/amu beam of ^{56}Fe beam with an initial width of 0.0 or 5.0 MeV/amu at various depths in an Aluminum target. The solid line is for numerical integration and the

broken line is for the analytic approximation in all these figures. The agreement for ^{40}Ca is excellent for all but the largest depth, while for ^{16}O the agreement is quite good only until about 50% of the range, and becomes progressively worse at larger depths. This is qualitatively typical for the $\mathbf{G}^2$ term. Calcium is relatively close to iron, in a fragmentation sense, so the agreement is quite good between the two approximations. On the other hand, in the same sense, oxygen is some distance from iron, so the agreement is

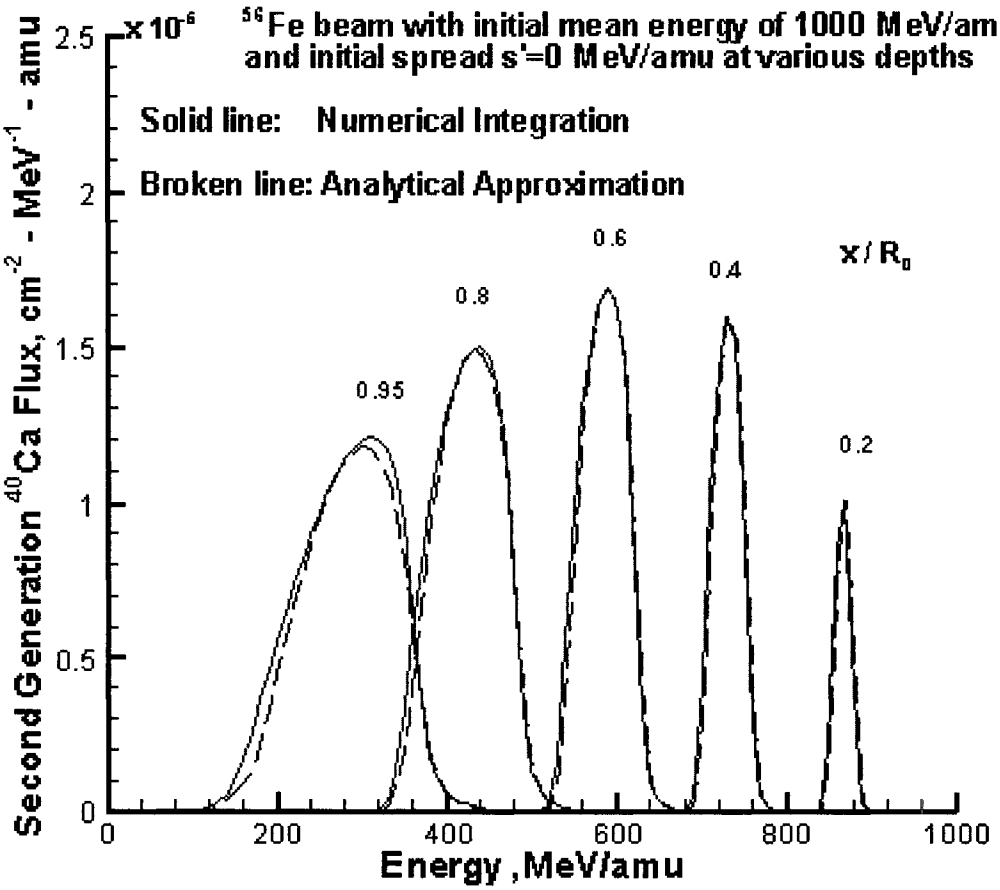

Fig. 7. Second generation ^{40}Ca fragment flux at various depths for the case $s' = 0$. The solid line is from numerical integration, and the broken line is the second order Green's function.

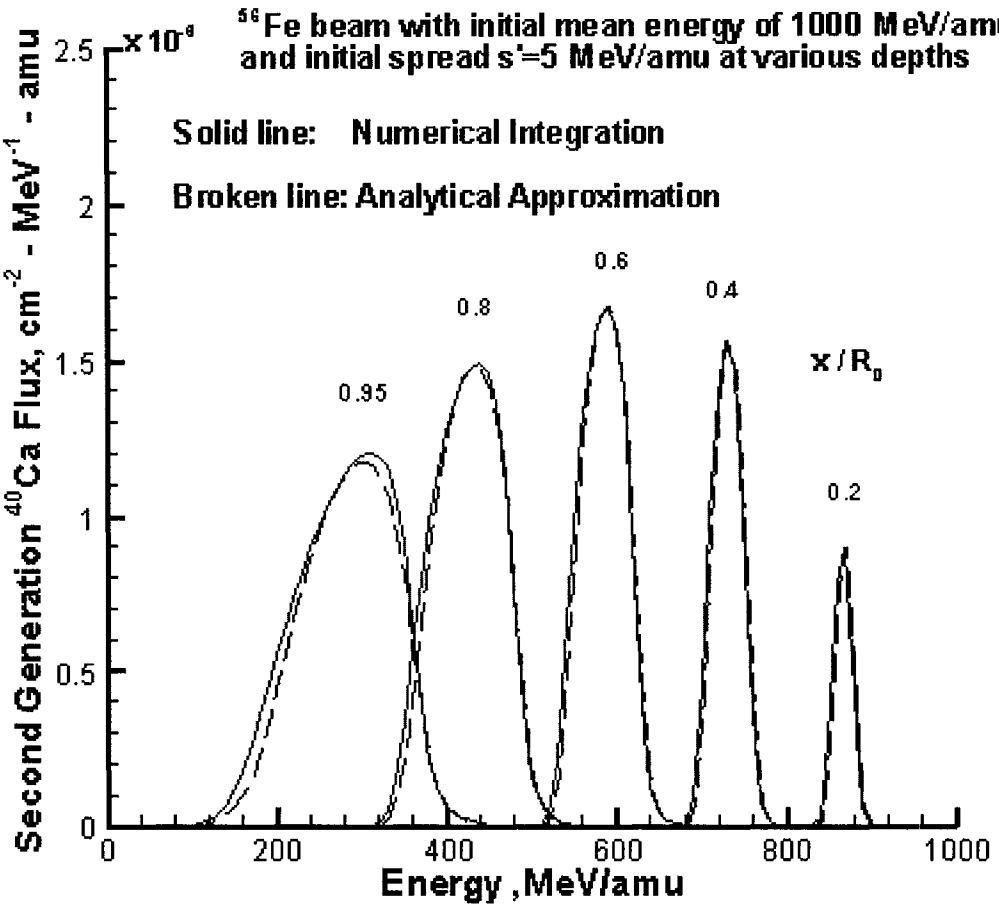

Fig. 8. Second generation ^{40}Ca fragment flux at various depths for the case $s' = 5$. The solid line is from numerical integration, and the broken line is the second order Green's function.

not as good. Overall though, the agreement is still highly acceptable.

Non-Perturbative Remainder

Nuclear cross sections are almost energy independent at very high energies, greater than 2 GeV/amu. This is true as long as the depth in question is not beyond the particles range; otherwise, the particle has been thermalized, brought to a complete stop in the material, and will not contribute. We define the integral fluences to be

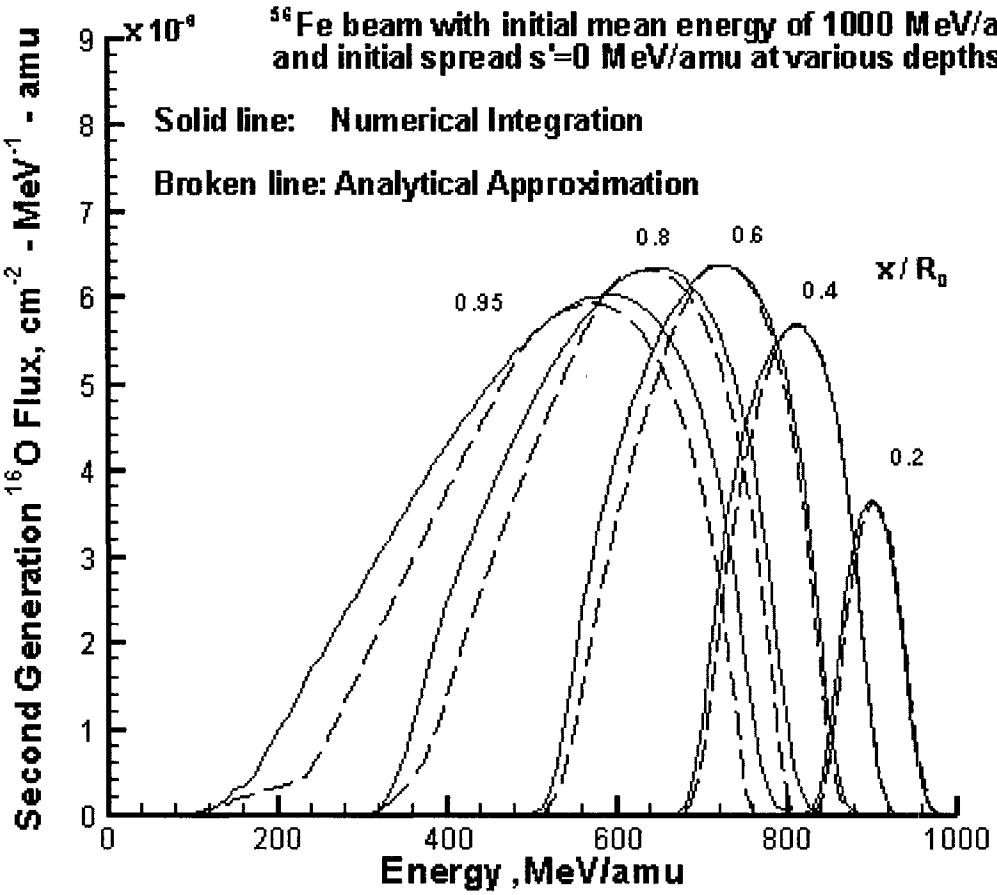

Fig. 9. Second generation ^{16}O fragment flux at various depths for the case $s' = 0$. The solid line is from numerical integration, and the broken line is the second order Green's function.

$$\bar{g}_{jk}(x-x') = \int G_{jk}(x,x',E,E')dE. \tag{4.41}$$

With this, if we integrate the Boltzmann equation (2.19), we get approximately

$$\left(\partial_x + \sigma_j\right)\bar{g}_{jk}(x-x') = \sum_p \sigma_{jp}\bar{g}_{pk}(x-x') \quad x' < x < x' + R_k(E'), \tag{4.42}$$

with $\bar{g}_{jk}(0) = \delta_{jk}$. This problem has been solved by Wilson et al. [21, 27, 28, 40], and the solution is

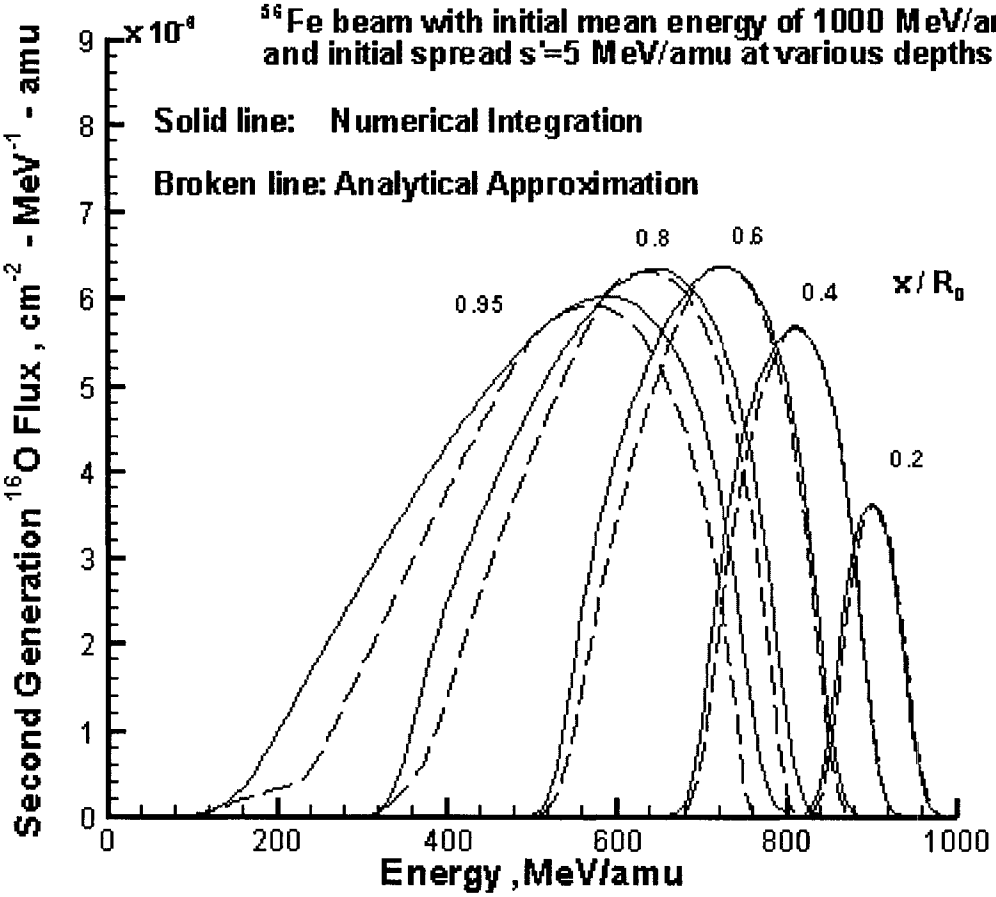

Fig. 10. Second generation ^{16}O fragment flux at various depths for the case $s' = 5$. The solid line is from numerical integration, and the broken line is the second order Green's function.

$$\overline{g}_{jk}(x-x') = \sum_{n=1}^{\infty} \overline{g}_{jk}^{(n)}(x-x') = \delta_{jk} g(k) + \sigma_{jk} g(j,k) + \sum_{p} \sigma_{jp}\sigma_{pk} g(j,p,k) + \cdots, \quad (4.43)$$

where the g-functions are found recursively via

$$g(i) = e^{-\sigma_i (x-x')}, \quad g(i_1,\ldots,i_n,i_{n+1}) = \frac{g(i_1,\ldots,i_{n-1},i_n) - g(i_1,\ldots,i_{n-1},i_{n+1})}{\sigma_{i_{n+1}} - \sigma_{i_n}}, \quad n \geq 1. \quad (4.44)$$

The integral fluences (4.41) are quite accurate at small depths, and can be extended to greater depths using the convolution formula [27, 40]

$$\overline{g}_{jk}(x-x') = \sum_{p} \overline{g}_{jp}(x-y)\overline{g}_{pk}(y-x') \quad x > y > x'. \tag{4.45}$$

For $n \geq 2$ there is little difference in the spectral shape of the fluences and we can make the simplifying assumption that

$$\frac{G_{jk}^{n}(x,x',E,E')}{\overline{g}_{jk}^{(n)}(x-x')} \approx \frac{G_{jk}^{2}(x,x',E,E')}{\overline{g}_{jk}^{(2)}(x-x')}. \tag{4.46}$$

With this the Neumann series remainder can be approximated by the non-perturbative expression

$$G_{jk}^{NP}(x,x',E,E') \approx \frac{G_{jk}^{2}(x,x',E,E')}{\overline{g}_{jk}^{(2)}(x-x')} \sum_{n} \overline{g}_{jk}^{(n)}(x-x') =$$

$$\frac{G_{jk}^{2}(x,x',E,E')}{\overline{g}_{jk}^{(2)}(x-x')} \left[\overline{g}_{jk}(x-x') - \overline{g}_{jk}^{(0)}(x-x') - \overline{g}_{jk}^{(1)}(x-x') - \overline{g}_{jk}^{(2)}(x-x') \right]. \tag{4.47}$$

Fig. 11 shows the first and second generation flux, and the non-perturbative remainder for ^{40}Ca fragments at various depths in aluminum for a 1000 MeV/amu Gaussian beam of ^{56}Fe with initial spread of 5.0 MeV/amu.

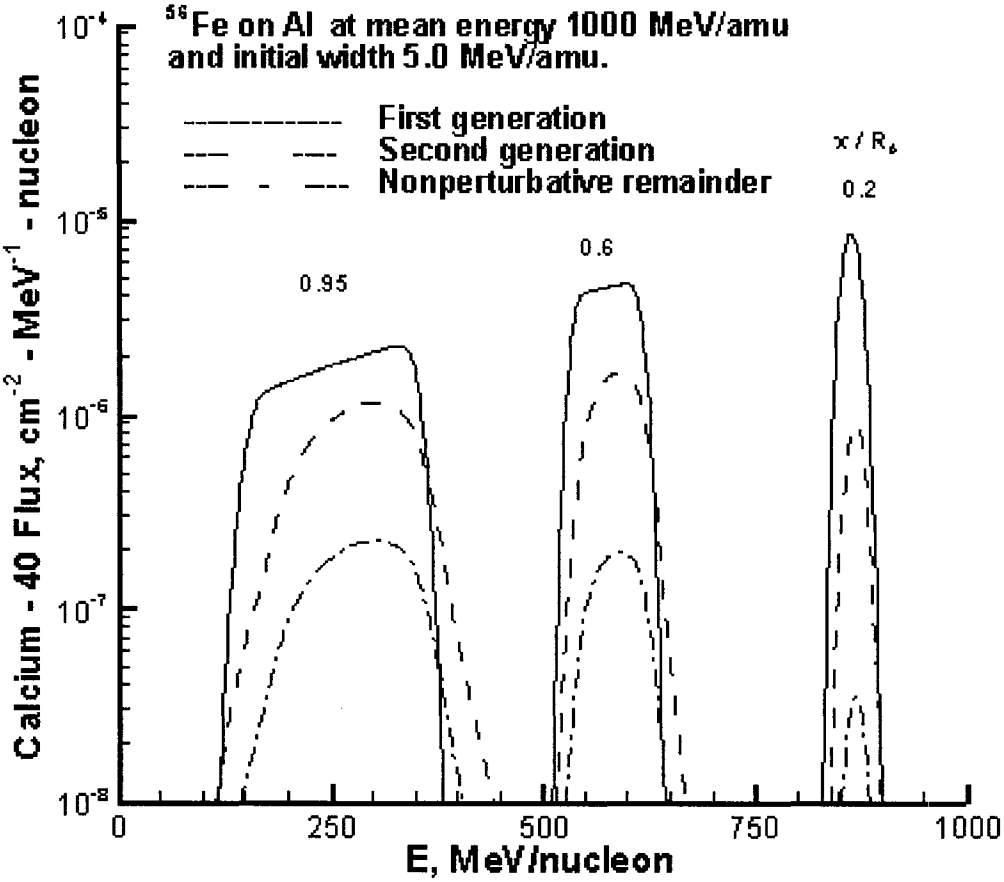

Fig. 11. First and second generation ^{40}Ca fragment flux and the non-perturbative reminder at various depths in Aluminum.

CHAPTER V

RESULTS AND COMPARISON WITH EXPERIMENTS

In order to validate the model, it is desirable to compare with actual experiments. Because of the extreme difficulty of testing materials in space, data from particle accelerators are used instead. Being able to make these comparisons is one of the strengths of this method. All calculations used the NUCFRG2 nuclear database [16, 25], which was based on the HZEFRG1 nuclear database, developed at the NASA Langley Research Center [15].

The light ions, z =1,2, have a strong angular dependence and there is a marked overprediction in their fluences. This is largely a consequence of the straightahead approximation because all particles produced are assumed to move parallel to the beam. Compounding the problem, the NUCFRG2 cross sections are somewhat inaccurate when it comes to the light ion multiplicities, meaning the same particle is created multiple times. If uncorrected, all the fluence data and everything derived from it would be incorrect, thereby making comparison to experiments meaningless. It is possible to correct for this by scaling $\phi_j(x,E)$ by an appropriate weight factor for each of the light ions, thereby reducing their number, and subsequent error. The weight factors are 0.02 for z =1 and 0.08 for z =2. These correction factors are empirically derived from comparisons with data reported by Miller et al. [41]. The corrections are incorporated into the fluence computations done by GRNTRN. Further refinement of the model will remove the need for these corrections.

Experimental Procedure

Since coming online in late 1995, a great deal of potential shielding and construction materials for space use had been tested at Brookhaven National Labs Alternating Gradient Synchrotron (BNL AGS) using ^{56}Fe as the incident ion. Iron was chosen because it is one of the heaviest ions that is present in large quantities in galactic cosmic rays (GCR), and thus has great biological significance. Typically for these experiments the beam energy extracted from the AGS was 1087 MeV/amu, and after passing through various upstream elements, had energy in the range of 1000-1050 MeV/amu before impacting the target.

A typical solid state detector setup is shown schematically in Fig. 12. This setup, and similar ones used by the same group, is detailed more extensively in [41-46]. The detectors upstream of the target were used to identify iron beam particles via energy

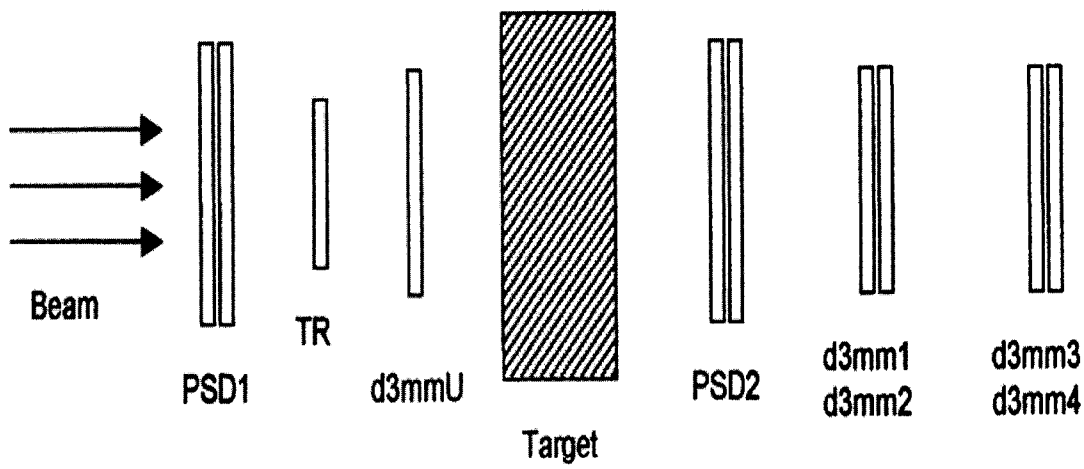

Fig. 12. Typical experimental detector setup (not to scale). All detectors are lithium drifted silicon; the trigger TR defines the size of the usable beam spot.

deposited. Data was recorded when an identified iron particle triggered a coincidence of signals in detectors TR and d3mmU. The trigger criterion was set to accept as many iron ions as possible, so fragments produced upstream within a few charges of iron also triggered events. These events, and instances where more than one iron ion passed through the system and was recorded, were eliminated in offline analysis. Once an event was triggered, the three pairs of detectors downstream of the target were used to determine fragment charges and energies. These detectors subtended small angles about the beam axis; a typical value for d3mm3 and d3mm4, collectively denoted as d3mm3/4, was 1°.

For each experimental setup, data is first taken without a target to measure the "background" fragmentation processes in order to eliminate this phenomenon from the gathered data. Runs without a target are called the "target out" runs. With or without a target, the experimental process is the same. For each event, position data is recorded from the two position detectors, PSD1 and PSD2; however this was subsequently not used in any analysis. Energy deposited in each detector, and additional high gain signals from d3mm1-4, used to identify the lighter ions, was also recorded.

Once the data was recorded and the background production eliminated, the resulting data was analyzed, in a method similar to that done previously [41- 46]. Scatterplots and histograms were made of the energy deposited, ΔE, in the detectors. The first set of graphical cuts eliminated the non-iron and multiple iron triggered events from the upstream detectors. The next set of cuts made sure that either a surviving iron beam, or one or more fragments, passed through each detector pair. A final series of cuts eliminated fragmentations occurring in the detectors downstream of the target. This

resulted in a series of peaks, primarily dominated by a single individual charge, and valleys in between. The small number of counts where adjacent peaks overlapped significantly was resolved utilizing double Gaussian fits to the adjacent peaks.

Detector Model

The detectors used are primarily made of lithium drifted silicon. As an ion passes through, one electron hole pair is liberated per 3.6 eV of the incident ion. The resulting current is then recorded for analysis. Thus the direct measurement is energy deposited in the detectors. These detectors have a 'dead layer', estimated to be 3%± 1.5% of the total detector thickness. The energy deposited here is lost, presumably to recombination. The additional energy loss of high energy beams due to the production of delta rays (high energy electrons) that escape the detector will be incorporated into the dead layer. All this energy lost will be modeled by using an effective detector thickness modified by the dead layer.

When a monoenergetic beam of j type particles of energy E' (MeV) and unit flux $\phi_j(0,E) = \delta(E - E')$ is incident on a silicon detector of effective thickness t (g/cm^2) the resulting flux is

$$\phi_j(t,E) = \frac{1}{\sqrt{2\pi}s_j(t,E')} \exp\left\{ -\frac{\left[E - E_j(t,E')\right]^2}{2s_j(t,E')^2} \right\}, \tag{5.1}$$

which is just the straggling form of the atomic Green's function, (3.10). A particle emerging with energy E has lost an amount of energy $E' = E' - E$. We define the unit spectral loss function $f_j(t,E',E')$ to be

$$\phi_j(t,E) = f_j(t,E^t,E') = \frac{1}{\sqrt{2\pi}s_j(t,E')}\exp\left\{-\frac{\left[E'-E^t-E_j(t,E')\right]^2}{2s_j(t,E')^2}\right\}. \quad (5.2)$$

Clearly, when incident flux is of a more general form $\phi_j(E)$, the emerging flux is given by

$$\phi_j(t,E) = F_j(t,E) = \int f_j(t,E^t,E')\phi_j(E')dE'. \quad (5.3)$$

In the special case of a Gaussian beam with initial spread s', (5.3) can be used to show the emerging flux to be approximately

$$F_j(t,E) = \frac{1}{\sqrt{2\pi}s_j'(t,E')}\exp\left\{-\frac{\left[E'-E^t-E_j(t,E')\right]^2}{2s_j'(t,E')^2}\right\}, \quad (5.4)$$

where

$$s_j'(t,E')^2 = s_j(t,E')^2 + s'^2 r_0(E_j)^2, \quad (5.5)$$

$r_0[E_j(t,E')] = 1 - S_j[E_j(t,E')]/S_j[E']$. Generally, the incident flux consists of the primary beam and all of its fragments, so the total energy deposited is

$$F(t,E^t) = \sum_{j=2}^{k} F_j(t,E^t). \quad (5.6)$$

The ion corresponding to the index $j=1$ in NUCFRG2 is the neutron, which is difficult for the detectors to measure, and is beyond the current theory here, and thus ignored.

Energy Deposited Comparisons

The numerical procedure for computing the energy deposited for any experiment is done as follows. First the fluence emerging from each target material was generated using the GRNTRN code. The resulting fluence was then fed to the detector model described above and an approximate dead layer correction factor (DLCF) was found. To compare with experiments, the subsequent numerical data was appropriately scaled and graphed along with the experimental data.

The first experiment to be compared to is a ^{56}Fe beam with initial energy extracted from the AGS at 1087 MeV/amu. The energy prior to striking the 7mm (1.89 g/cm^2) of Aluminum target was 1037 MeV/amu [41]. The beam spread prior to impact is not known, but data from similar experiments done within months of this one quote a spread of 5 MeV/amu [43], consequently this value was used for the impact spread. Fig. 13 shows energy deposited in the d3mm3 and d3mm4 detectors from the experiment

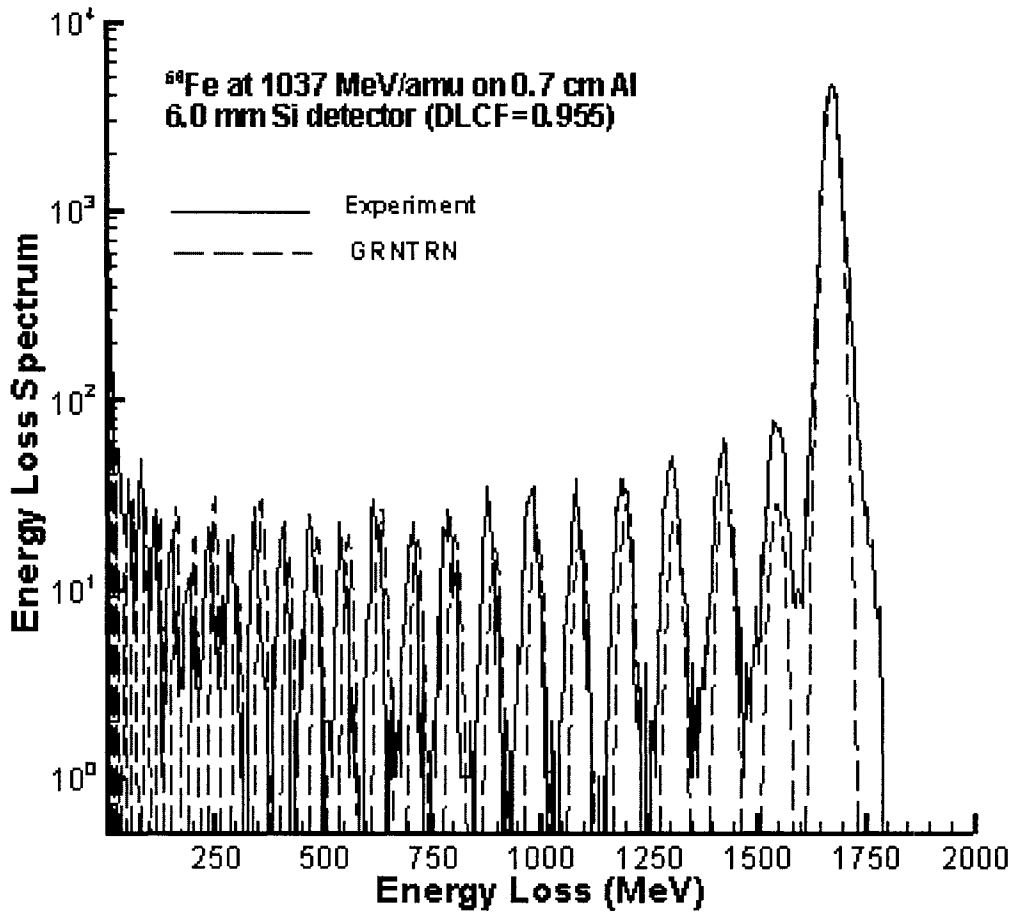

Fig. 13. Energy loss spectrum for 1037 MeV/amu ^{56}Fe beam with spread of 5 MeV/amu striking 7mm of Al as measured in detectors d3mm3/4. The solid line is experimental measurements and the dashed line is model computations. The DLCF was found to be 0.955.

(solid line) and computed energy loss spectrum (dashed line). The DLCF was found to be 0.955, within the accepted range for these detectors. The rightmost peak in Fig. 13 is dominated by all ions with z =26. The next peak to the left is dominated by z =25, Manganese, followed by z =24, Chromium, and so forth. The contributions for z =10 and greater can clearly be seen. The Manganese peak is much lower than the experimental results, reflecting a known weakness in the NUCFRG2 cross sections [43]. The peak for Vanadium, z =23, is also lower than expected. The computed peaks failing to line up as we move to the right indicates that the simple model for computing energy downshift due to fragmentation could use some refinement for large mass removal. Further, it has been reported by Miller et al. [43], that the cross section for Aluminum generated by NUCFRG2 is not as good as for other tested target elements. Overall though, the agreement is quite acceptable.

Fig. 14 displays the results for a ^{56}Fe beam with an energy of 1050 MeV/amu and assumed spread of 5 MeV/amu just prior to impact on 10 g/cm^2 of 50.92/ 49.08% Graphite-Epoxy mix [42]. As with Fig. 13, the Manganese peak has the greatest disparity between experiment and computation. The rest of the peaks are closer to the experimental values here than for Fig. 13, suggesting that because the Graphite-Epoxy mix consists of fair number of elements, errors in cross sections for one element may be smoothed out for multi-element compounds. The energy downshift also is much more accurate than for Aluminum. The only concern is that the DLCF is found to be 0.95, just slightly below the lowest believed value of 0.955. This may be due to ignoring elastic scattering effects, which would lower the overall average energy, resulting in more energy being deposited by each particle, thus raising the DLCF.

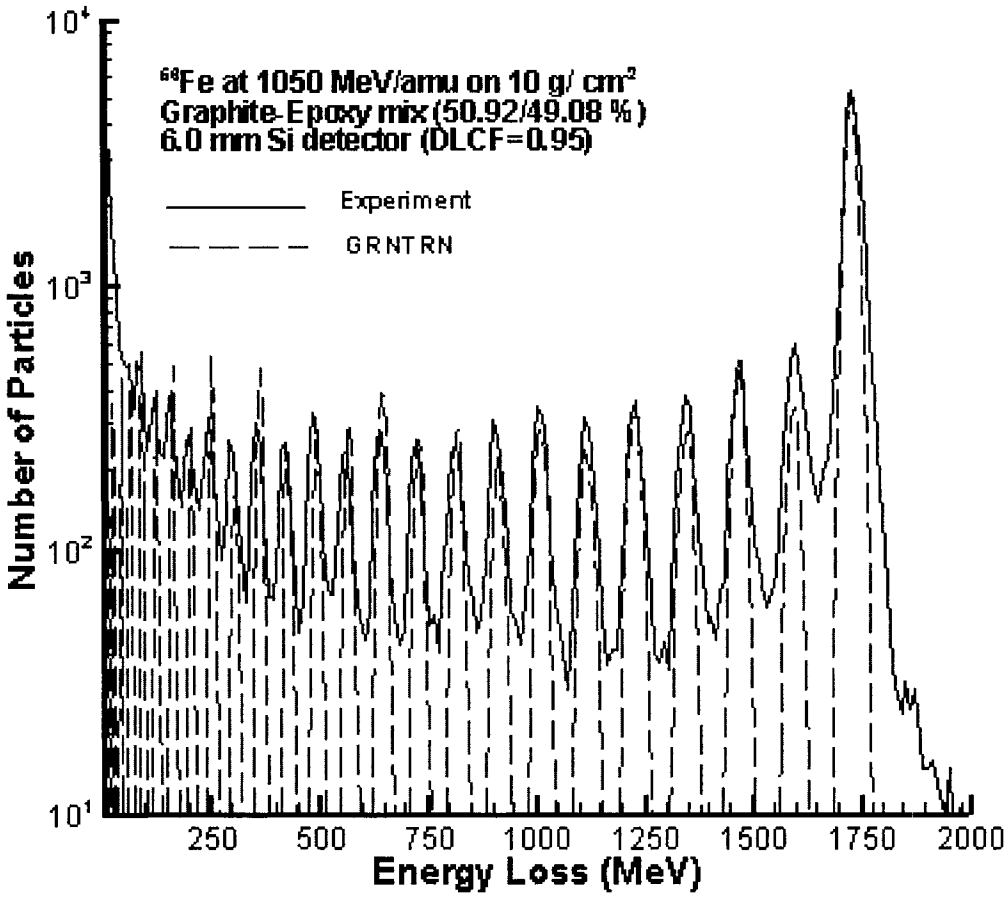

Fig. 14. Energy loss spectrum for 1050 MeV/amu ^{56}Fe beam with spread of 5 MeV/amu striking 10 g/cm^2 of 50.92/49.08 % Graphite-Epoxy mix, as measured in detectors d3mm3/4. The solid line is experimental measurements and the dashed line is model computations. The DLCF was found to be 0.95.

Fraction of Primary Beam Surviving

In addition to being able to record energy losses, the detectors are able to determine the charge of the ion depositing the energy. This allows the contribution sorted by charge of many quantities of interest. One of the most basic of these quantities is the fluence spectrum. It is very common for experimentalists to report the "fraction of primary beam surviving", especially when they do not report the entire fragment spectra.

What they mean is all of the ions emerging from the target with the same charge as the primary beam. Depending on the element used, a primary beam ion can lose one or more neutrons passing through the target. For example, all the experiments that will be compared to have ^{56}Fe as the primary ion. What emerges from the target with z =26 is predominately ^{56}Fe, with a small amount of ^{55}Fe and ^{54}Fe. Using the NUCFRG2 database, the model can make this isotopic distinction, but experiments cannot. The fraction of type i ions surviving can be found by

$$F_{surviving} = \int_0^{E'} \phi_i(x, E)dE. \tag{5.7}$$

Table 1 lists the fraction of iron surviving for several different materials. The first line consists of data reported by Miller el al. [41], and is the same experiment represented in Fig. 13, while the rest of Table 1 is experimental data consisting of preliminary results from the BNL AGS [47]. The exact beam characteristics just prior to impacting the various targets are not known; what is known is that the energy was around 1 GeV/amu and the impact spread was small. The unknown experiments were modeled with impact energy of 1000 MeV/amu and zero initial width. The model and the experiments agree quite well; the largest error is for 5 g/cm^2 Graphite-Epoxy mix and is less than 6%.

Table 2 has the comparisons between calculations and preliminary experimental results from runs done in June 2004 [48]. As before, the experiments were modeled with impact energy of 1000 MeV/amu and zero initial spread. The reason for separating the results is twofold. First, all the runs for Table 1 were done within a year or so of each other, many years previous to the runs for Table 2. Second, and most importantly, the results for Table 2 are from the detector set closest to the target (analogous to the d3mm1/2 detectors). Experimentalists compute the fraction of primary surviving by

finding the percentage of primary ions recorded in the detector pair and then applying a correction factor found from the target out runs for the small number of primary fragmentations that occur in the detector pair. While the correction for moving from the d3mm1/2 detector pair to the d3mm3/4 detector pair is believed to be small, it is unclear as to whether the change will bring the experimental results closer to model predictions, or farther away. Currently the largest error in Table 2 is 4.5%, and the change is not expected to make things any worse than the 6% error of Table 1.

Table 1
Comparison between model calculations and preliminary experimental results for the fraction of primary ion surviving as measured in the detector pair farthest downstream from the target.

Material	Material Thickness (g/cm^2)	Fraction of Iron surviving: Model	Fraction of Iron surviving: Experiment
Aluminum	1.89	.914	.93
Carbon	3.9	.711	.737
Aluminum	7	.719	.733
Lead	3.6	.926	.959
Polyethylene	10	.300	.300
Graphite-Epoxy	5	.635	.673
Graphite-Epoxy	10	.416	.427
Pure Epoxy	1.3	.878	.888
Copper	11.3	.751	.741
Copper	6.13	.859	.830

Track Average LET

Linear energy transfer, LET, is the energy deposited in the attenuating material per unit path length of incident radiation, and is measured in units of keV/μm. LET and track average LET, $<LET>_{trk}$, indirectly give a measure of health risk for people that the primary ion and its fragments pose after emerging from a target to a person if they were

Table 2
Comparison between model calculations and preliminary experimental results for the fraction of primary ion surviving as measured in the detector pair closest downstream for various targets.

Material	Material Thickness (g/cm^2)	Fraction of Iron surviving: Model	Fraction of Iron surviving: Experiment
Ultem	5.01	.632	.633
UDABDA1	4.87	.631	.636
Clay Epoxy	4.96	.599	.627
DDS Epoxy	4.86	.636	.641
AFDA Epoxy	5.14	.560	.585
Beryllium	5.05	.604	.602
AM162	5.49	.644	.640
AM140	6.38	.649	.638
Graphite, LDK1V9	4.07	.718	.733
Graphite Foam	4.61	.686	.698
C-C Composite	5.31	.646	.659

right behind the target. Calculations derived from LET are typically used in measures of risk by biologists. Computed from the $<LET>_{trk}$ are the dose, dose equivalent, and quality factors used to measure radiation risk. If the track average LET is found to be correct, then the derived quantities will be correct. The $<LET>_{trk}$ can be computed from the formula

$$\langle LET\rangle_{trk} = \sum_i \int L_i(E)\phi_i(x,E)dE \Big/ \sum_i \int \phi_i(x,E)dE\,, \tag{5.8}$$

where $\phi_i(x,E)$ is the flux and $L_i(E)$ is the LET of the i^{th} particle type at energy E. In order to be able to make comparisons with experimental data, we will take $L_i(E)$ to be LET_∞ in water for particle i at energy E; i.e., the stopping power, $S_i(E)$, for water. Water is used because there are extensive published tables of the stopping power in water for many ions and neutrons at various energies.

Table 3 lists the $<LET>_{trk}$ for the same materials represented in Table 1, and also

includes published results for various thickness of polyethylene [44]. The agreement between experiments and model predictions are very good; most errors are very small, under 4%, with 11.3 g/cm^2 of copper having the largest error of 7%. Table 4 has the analogous results for the materials from Table 2. The fact that the computed $<LET>_{trk}$ for materials in Table 4 is lower than experimental findings is encouraging. From previous experiments [41], it is known that the $<LET>_{trk}$ will decrease from detectors d3mm1/2 to detectors d3mm3/4. While the exact decrease depends on the target material and thickness, and is not known, it would reduce the overall error, thereby improving comparisons.

Table 3
Comparison of computed track average LET with experimental results from detectors farthest downstream of the various targets.

Material	Material Thickness (g/cm^2)	$<LET>_{trk}$ Model $(keV/\mu m)$	$<LET>_{trk}$ Experiment $(keV/\mu m)$
Aluminum	1.89	143.0	140
Polyethylene	1.94	133.9	135
Polyethylene	4.68	114.2	117
Polyethylene	9.35	93.5	95
Carbon	3.9	125.5	127.0
Aluminum	7	127.1	125.4
Lead	3.6	148.2	145.8
Polyethylene	10	92.3	91.4
Graphite-Epoxy	5	119.4	121.3
Graphite-Epoxy	10	98.7	98.5
Pure Epoxy	1.3	141.5	139.3
Copper	11.3	132.5	123.8
Copper	6.13	140.1	135.3

Table 4
Comparison of computed track average LET with experimental results from detectors closest downstream of the various targets.

Material	Material Thickness (g/cm^2)	$<LET>_{trk}$ model $(keV/\mu m)$	$<LET>_{trk}$ experiment $(keV/\mu m)$
Ultem	5.01	118.1	122.1
UDABDA1	4.87	118.1	121.9
Clay Epoxy	4.96	115.7	122.5
DDS Epoxy	4.86	119.5	123.4
AFDA Epoxy	5.14	114.0	119.6
Beryllium	5.05	109.4	116.1
AM162	5.49	114.9	120.3
AM140	6.38	116.7	120.3
Graphite, LDK1V9	4.07	124.3	129.0
Graphite Foam	4.61	121.2	126.7
C-C Composite	5.31	117.2	122.6

CHAPTER 6

CONCLUSIONS AND FUTURE WORK

In this work, a concise theory for ion transport has been developed. The Boltzmann transport equation was reduced to one dimension using the straightahead approximation. Common perturbation expansions were introduced, making the solution of Boltzmann's equation a series of related problems. The Green's function problem was formulated and the first three terms of the Neumann solution were derived. Each of these terms included energy dependent nuclear cross sections, energy downshift, collision interaction widths, and energy straggling. A non-perturbative remainder was used to complete the series.

Based on this solution a new version of GRNTRN, a code designed for comparison with laboratory experiments, using the NUCFRG2 nuclear database, was written. Data derived from GRNTRN was then compared to a large number of experiments done at the Brookhaven National Laboratory Alternating Gradient Synchrotron using a beam of ^{56}Fe ions. The results were extremely good overall, which is encouraging when taking into account the large number of targets of various thickness used.

Despite the success, there are still key areas for future work. First, the addition of nuclear elastic scattering must be addressed. The inclusion of elastic scattering would help raise the DLCF and broaden out the peaks in comparisons with energy deposited in detectors. Elastic scattering would also incorporate more angular dependence into this model, and potentially eliminate the need, or at least provide a theoretical basis, for the

angular correction factors for Hydrogen and Helium ions. Extending the results to multilayer/ nonuniform materials would have great impact on modeling space structures like the International Space Station, future space suits and the next generation space shuttle.

Unrelated to the model itself, but also a potential improvement in accuracy, is in the choice of nuclear data used. At present, NUCFRG2 is being used to generate the nuclear cross sections. Currently in development by F. A. Cucinotta is QMSFRG, a quantum multiple scattering fragmentation model [43]. Preliminary experiments demonstrate QMSFRG's accuracy over NUCFRG2, with further planned refinements expected to increase this accuracy [43]. Once QMSFRG is fully developed, GRNTRN should be converted to use the improved nuclear data and comparison made between the model results here using NUCFRG2 and those based on QMSFRG. All in all, the potential exists for years of research.

REFERENCES

[1] J.W. Wilson, L.W. Townsend, W. Schimmerling, G.S. Khandelwal, F. Khan, J.E. Nealy, F.A. Cucinotta, L.C. Simonsen, J.L. Shinn, J.W. Norbury, Transport Methods and Interactions for Space Radiations, NASA RP-1257, National Aeronautics and Space Administration, 1991.

[2] A.H. Hillas, Cosmic Rays, Pergamon Press, Ltd., New York, 1972.

[3] P. Freier, E.J. Lofgren, E.P. Ney, F. Oppenheimer, H.L. Bradt, B. Peters, Evidence for heavy nuclei in the primary cosmic radiation, Phys. Rev. vol. 74, no. 2 (1948) 213-217.

[4] P. Freier, E.J. Lofgren, E.P. Ney, F. Oppenheimer, The heavy component of primary cosmic rays, Phys. Review, vol. 74 (2), no.12 (1948) 1818-1827.

[5] H. Armstrong, H. Haber, H. Strughold, Aero Medical Problems Space Travel-Planning Meeting, School of Aviation Medicine, in: J. Aviation Med. 20 (1949) 384-417.

[6] H.J. Schaefer, Evaluation of present-day knowledge of cosmic radiation at extreme altitude in terms of hazard to health, J. Aviation Med. 21 (1950) 375-394.

[7] J.G. Jacobs, ed., Proceedings of Conference on Radiation Problems in Manned Space Flight, NASA TN D-588, National Aeronautics and Space Administration, 1960.

[8] J.L. Shinn, J.W. Wilson, M. Weyland, F.A. Cucinotta, Improvements in Computational Accuracy of BRYNTRN (A Baryon Transport Code), NASA TP-3093, National Aeronautics and Space Administration, 1991.

[9] J.W. Wilson, L.W. Townsend, J.E. Nealy, S.Y. Chun, B.S. Hong, W.W. Buck, S.L. Lamkin, B.D. Ganapol, F. Khan, F.A. Cucinotta, BRYNTRN: A Baryon Transport Model, NASA TP-2887, National Aeronautics and Space Administration, 1989.

[10] J.W. Wilson, Analysis of the Theory of High Energy Ion Transport, NASA TN D-8381, National Aeronautics and Space Administration, 1977.

[11] J.W. Wilson, Heavy ion transport in the straightahead approximation, NASA TP-2178, National Aeronautics and Space Administration, 1983.

[12] J. W. Wilson, F.F. Badavi, Methods of galactic heavy ion transport, Radiat. Res. 108 (1986) 231-237.

[13] J.W. Wilson, S.Y. Chun, F.F. Badavi, L.W. Townsend, S.L. Lamkin, HZETRN: A Heavy Ion/ Nucleon Transport Code for Space Radiation, NASA TP-3146, National Aeronautics and Space Administration, 1991.

[14] J.W. Wilson, F.F. Badavi, F.A. Cucinotta, J.L. Shinn, G.D. Badhwar, R. Silberberg, C.H. Tsao, L.W. Townsend, R.K. Tripathi, HZETRN: Description of a Free-Space Ion and Nucleon Transport and Shielding Computer Program, NASA TP-3495, National Aeronautics and Space Administration, 1995.

[15] L.W. Townsend, J.W. Wilson, R.K. Tripathi, J.W. Norbury, F.F. Badavi, F. Khan, HZEFRG1: An Energy-Dependent Semiemperical Nuclear Fragmentation Model, NASA TP-3310, National Aeronautics and Space Administration, 1993.

[16] J.W. Wilson, J.L. Shinn, L.W. Townsend, R.K. Tripathi, F.F. Badavi, S.Y.Chan, NUCFRG2: A simiemperical nuclear fragmentation model, Nucl. Instrum. Meth. B 94 (1994) 95-102.

[17] J.W. Wilson, L.W. Townsend, H.B. Bidasoria, W. Schimmerling, M. Wong, J. Howard, ^{20}Ne depth-dose relationship in water, Health Phys. 45 (5) (1984) 1101-1111.

[18] W. Shimmerling, J. Miller, M. Wong, M. Rapkin, J. Howard, H.G. Speiler, B.V. Jarret, The fragmentation of 670 A MeV Neon-20 as a function of depth in water, Radiat. Res. 120 (1989) 36-71.

[19] W. Schimmerling, J. Howard, M. Rapkin, M. Wong, The propagation of relativistic heavy ions in multi-element beam lines, Med. Phys. 13 (1986) 217-228.

[20] J.W. Wilson, S.L. Lamkin, B.D. Ganapol, A closed form solution to HZE propagation, Radiat. Res. 122 (1990) 223-228.

[21] J.W. Wilson, S.L. Lamkin, H. Farhat, B.D. Ganapol, L.W. Townsend, A Hierarchy of Transport Approximations for High Energy (HZE) Ions, NASA TM-4118, National Aeronautics and Space Administration, 1989.

[22] J.W. Wilson, Depth-Dose Relations for heavy ion beams, Virginia J. Sci. 28 (3) (1977) 136-138.

[23] J.W. Wilson, F.A. Cucinotta, J.L. Shin, L.C. Simonsen, F.F. Badavi, Overview of HZETRN and BRYNTRN space radiation shielding codes, SPIE 2881 (1996) 51-62.

[24] S.Y. Chun, Dosimetry of high-energy heavy-ion beams using energy-dependent Green's functions, Ph. D. Dissertation, Old Dominion University, September 1994.

[25] J.W. Wilson, R.K. Tripathi, F.A. Cucinotta, J.L. Shinn, F.F. Badavi, S.Y. Chun, J.W. Norbury, C.J. Zeitlin, L. Heilbronn, J. Miller, NUCFRG2: An evaluation of the semiemperical nuclear fragmentation database, NASA TP-3533, National Aeronautics and Space Administration, 1995.

[26] J.L. Shinn, S. John, R.K. Tripathi, J.W. Wilson, L.W. Townsend, J.W. Norbury, Fully Energy-Dependent HZETRN (A Galactic Cosmic-Ray Transport Code), NASA TP-3243, National Aeronautics and Space Administration, 1992.

[27] J.W. Wilson, F.F. Badavi, R.C. Costen, J.L. Shinn, Nonperturbative Methods in HZE Ion Transport, NASA TP-3363, National Aeronautics and Space Administration, 1993.

[28] J.W. Wilson, R.C. Costen, J.L. Shinn, F.F. Badavi, Green's Function Methods in Heavy Ion Shielding, NASA TP-3311, National Aeronautics and Space Administration, 1993.

[29] J.L. Shinn, J.W. Wilson, E.V. Benton, F.F. Badavi, Multilayer analysis of an Iron radiation beam experiment, NASA TM-4753, National Aeronautics and Space Administration, 1997.

[30] S.Y. Chun, G.S. Khandelwal, J.W. Wilson, A Green's function method for high charge and energy ion transport, Nucl. Sci. Eng., 122 (1996) 267-275.

[31] R.K. Tripathi, L.W. Townsend, F Kahn, Role of intrinsic width in fragment momentum distributions in heavy ion collisions, Phys. Rev. C, 48 (4) (1994) 1775-1777.

[32] J.W. Wilson, J. Tweed, H. Tai, R.K. Tripathi, A simple model for straggling evaluation, Nucl. Instr. Methods Phys. Res. B 194 (2002) 389-392.

[33] J. Tweed, J.W. Wilson, R.K. Tripathi, A fundamental solution of the linear Boltzmann equation, presented at: Space Radiation Shielding Technology Workshop, NASA Langley Research Center, Hampton, VA, April, 2002.

[34] J. Tweed, J.W. Wilson, R.K. Tripathi, An improved Green's function for ion beam, Adv. Sp. Res. 34 (6) (2004) 1311-1318.

[35] J.H. Heinbockel, Introduction to Tensor Calculus and Continuum Mechanics, Trafford Publishing, Victoria, B.C., 2001.

[36] J.L. Shin, H. Farhat, F.F. Badavi, J.W. Wilson, Polarization Correction for Ionization Loss in a Galactic Cosmic Ray Transport Code (HZETRN), NASA TM-4443, National Aeronautics and Space Administration, 1993.

[37] R.G. Alsmiller Jr., D.C. Irving, W.E. Kinney, H.S. Moran, The validity of the straightahead approximation in space vehicle shielding studies, in: A. Reetz, Jr. (Ed.), Second Symposium on Protection Against Radiation in Space, NASA SP-71, National Aeronautics and Space Administration, 1965 pp. 177-181.

[38] R.G. Alsmiller Jr., D.C. Irving, H.S. Moran, Validity of the straightahead approximation in spacevehicle shielding studies, Part II, Nucl. Sci. Eng. 32 (1) (1969) 56-61.

[39] J.W. Wilson, S.L. Lamkin, Perturbation theory for charged-particle transport in one dimension, Nuclear Sci. & Eng. 57 (4) (1975) 292-299.

[40] J.W. Wilson, M.R. Shavers, F.F. Badavi, J. Miller, Nonperturbative methods in HZE propagation, Radiat. Res 140 (2) (1994) 241-248.

[41] J. Miller, C. Zeitlin, F.A. Cucinotta, L. Heilbronn, D. Stephens, J.W. Wilson, Benchmark studies of the effectiveness of structural and internal materials as radiation shielding for the International Space Station, Radiat. Res. 159 (2003) 381-390.

[42] J. Miller, Laboratory validation of material shielding properties, in: Shielding Stratagies for Human Space Exploration, NASA CP-3360, National Aeronautics and Space Administration, 1998, pp. 427-433.

[43] C. Zeitlin, L. Heilbronn, J. Miller, S.E. Rademacher, T. Borak, T.R. Carter, K.A. Frankel, W. Shimmerling, C.E. Stronach, Heavy fragment production cross sections from 1.05 GeV/ nucleon ^{56}Fe in C, Al, Cu, Pb, and CH_2 targets, Physical Rev. C 56 (1) (1997) 388-397.

[44] C. Zeitlin, L. Heilbronn, J. Miller, Detailed Charaterization of the 1087 MeV/ nucleon Iron-56 beam used for radiobiology at the Alternating Gradient Synchrotron, Rad. Res. 149 (1998) 560-569.

[45] C. Zeitlin, J. Miller, L. Heilbronn, K. Frankel, W. Gong, W. Shimmerling, The fragmentation of 510 MeV/ nucleon Iron-56 in polyethylene. I. Fragment fluence spectra, Radiat. Res. 145 (1996) 655-665.

[46] C. Zeitlin, A. Fukumura, L. Heilbronn, Y. Iwata, J. Miller, T. Murakami, Fragmentation cross sections of 600 MeV/ nucleon ^{20}Ne on elemental targets, Phys. Rev. C 64 (2001) 024902.

[47] J. Miller, 2003, private communication.

[48] S. Guetersloh, 2004, private communication.

VITA

Steven Andrew Walker was born on May 8, 1974 at Fort Ord Army Hospital, Monterey, California. He is the oldest of three sons born to Lieutenant Commander Charles Harrison Walker, U.S. Navy (ret.) and Evleen Margaret Walker. He graduated from Old Dominion University in 1996. After what was supposed to be a brief vacation, he returned to ODU on a part time basis in 1999 to pursue a graduate degree. In 2000 he became a full time student and teaching assistant. In 2002 he became a research assistant, a position he has held ever since. He received his Ph. D. in Computational and Applied Mathematics in May 2005.